Optical harmonic generation in monolayer group-VI transition metal dichalcogenides

Anton Autere,[1] Henri Jussila,[1] Andrea Marini,[2] J. R. M. Saavedra,[2] Yunyun Dai,[1] Antti Säynätjoki,[1,3] Lasse Karvonen,[1] He Yang,[1] Babak Amirsolaimani,[4] Robert A. Norwood,[4] Nasser Peyghambarian,[1,3,4] Harri Lipsanen,[1] Khanh Kieu,[4] F. Javier García de Abajo,[2,5] and Zhipei Sun[1,6,*]

[1]*Department of Electronics and Nanoengineering, Aalto University, P.O. Box 13500, FI-00076 Aalto, Finland*
[2]*ICFO-Institut de Ciències Fotòniques, The Barcelona Institute of Science and Technology, 08860 Castelldefels, Barcelona, Spain*
[3]*Institute of Photonics, University of Eastern Finland, Yliopistokatu 7, FI-80101 Joensuu, Finland*
[4]*College of Optical Sciences, University of Arizona, 1630 East University Boulevard, Tucson, Arizona 85721, USA*
[5]*ICREA-Institució Catalana de Recerca i Estudis Avançats, Passeig Lluís Companys 23, 08010 Barcelona, Spain*
[6]*QTF Centre of Excellence, Department of Applied Physics, Aalto University, FI-00076 Aalto, Finland*

(Received 30 October 2017; revised manuscript received 10 August 2018; published 17 September 2018)

Monolayer transition metal dichalcogenides (TMDs) exhibit high nonlinear optical (NLO) susceptibilities. Experiments on MoS_2 have indeed revealed very large second-order ($\chi^{(2)}$) and third-order ($\chi^{(3)}$) optical susceptibilities. However, third-harmonic generation results of other layered TMDs have not been reported. Furthermore, the reported $\chi^{(2)}$ and $\chi^{(3)}$ of MoS_2 vary by several orders of magnitude, and a reliable quantitative comparison of optical nonlinearities across different TMDs has remained elusive. Here, we investigate second- and third-harmonic generation, and three-photon photoluminescence in TMDs. Specifically, we present an experimental study of $\chi^{(2)}$ and $\chi^{(3)}$ of four common TMD materials (MoS_2, $MoSe_2$, WS_2, and WSe_2) by placing different TMD flakes in close proximity to each other on a common substrate, allowing their NLO properties to be accurately obtained from a single measurement. $\chi^{(2)}$ and $\chi^{(3)}$ of the four monolayer TMDs have been compared, indicating that they exhibit distinct NLO responses. We further present theoretical simulations of these susceptibilities in qualitative agreement with the measurements. Our comparative studies of the NLO responses of different two-dimensional layered materials allow us to select the best candidates for atomic-scale nonlinear photonic applications, such as frequency conversion and all-optical signal processing.

DOI: 10.1103/PhysRevB.98.115426

I. INTRODUCTION

Recent years have witnessed a growing interest in two-dimensional (2D) layered materials for various electronic and photonic applications [1]. These 2D materials include graphene [2] and transition metal dichalcogenides (TMDs), especially molybdenum disulfide (MoS_2) [3–5]. TMDs possess fascinating layer-dependent optical and electrical properties, such as their layer-dependent band gap. For example, bulk (group-VI) TMDs are typically indirect band-gap semiconductors, while in single atomic layers their band gap becomes direct in the ∼1.55–1.9 eV range [3,4,6]. This renders monolayer TMDs (ML-TMDs) as attractive materials for various optoelectronic applications, such as light-emitting devices, detectors, and modulators [5,7]. ML-TMDs consist of two hexagonal lattices of chalcogen atoms separated by a plane of metal atoms occupying trigonal prismatic sites between the chalcogens [5]. Owing to their crystal structure, TMDs with an odd number of layers are noncentrosymmetric, while TMDs in bulk or with any even number of layers are centrosymmetric [8]. The lack of inversion symmetry in ML-TMDs leads to substantial second-order nonlinear optical susceptibility $\chi^{(2)}$.

Nonlinear optical (NLO) processes in 2D materials are of great interest for various technological applications [9–14], such as frequency conversion, all-optical signal processing, ultrafast pulse generation, and parametric sources of quantum photon states. Furthermore, integration of 2D materials with photonic integrated circuits offers exciting prospects for new applications. In particular, it has already been shown that the NLO responses of 2D materials can be enhanced with waveguides [9,15] and photonic crystal structures [9,10,16]. The NLO properties of 2D materials are promising for the development of on-chip devices, such as nonlinear light sources for quantum photonics and metrology or nonlinear phase modulation devices [9,17]. In addition, the fundamental properties (e.g., crystal orientation) of different 2D materials can be probed via nonlinear optical processes such as second-harmonic generation (SHG), which is important for nanomaterial characterization [9,18–20]. Thus far, research on TMDs has been focused on their electronic and linear-optical properties, with only few studies reporting on NLO properties. Several groups have already reported the observation of SHG in mono- and trilayer MoS_2 [8,21–23], as well as in $MoSe_2$ [24], WS_2 [25], and WSe_2 [26]. Additionally, third-order optical nonlinearity, quantified through the third-order susceptibility $\chi^{(3)}$, has been recently observed in few-layer [27] and monolayer [28–30] MoS_2.

The rapid advance of the field has led to the observation of high-harmonic generation (HHG) in ML MoS_2 under intense laser excitation [31]. However, there are several aspects of the NLO response of TMDs that remain unexplored. For

*zhipei.sun@aalto.fi

example, nonlinear optics with other TMDs [e.g., third-harmonic generation (THG) in WSe_2, $MoSe_2$, and WS_2] has not been fully studied [9]. Furthermore, there is a large deviation in reported experimental values of $\chi^{(2)}$ for 2D materials (including TMDs), which could be partially attributed to differences between measurement conditions (e.g., excitation conditions, sample doping, and strain effects) in those studies and also to the different substrates used in the measurements (e.g., different thicknesses and compositions). In fact, especially in the case of 2D materials, the substrate has a significant impact on harmonic generation [32–34], which makes the comparison of $\chi^{(2)}$ and $\chi^{(3)}$ values from different measurements problematic. For example in MoS_2, the reported values of $|\chi^{(2)}|$ at 800 nm excitation vary from 10^{-7} to 10^{-10} m V^{-1} (i.e., by three orders of magnitude) [8,21,22]. Furthermore, different experimental methods, such as two-wave mixing [35], multiphoton microscopy [18,28,29], and spatial self-phase modulation [17,36], have been used to quantify the nonlinear susceptibilities of different materials, thus making the comparison even more involved. In conclusion, despite the importance of accurately assessing the NLO susceptibilities of TMDs and shedding light on their dependence on environmental conditions (e.g., as a tool to modulate the response at will), experimental studies so far available are fragmented and do not allow us to establish a systematic comparison between different materials.

Here, we present an experimental study of the second- and third-order NLO properties of group-VI TMDs that is immune to differences in sample and excitation conditions. Monolayers of the four TMD materials MoS_2, $MoSe_2$, WS_2, and WSe_2 are mechanically exfoliated and transferred onto a substrate, in close proximity to each other using a state-of-the-art dry-transfer technique. The effective NLO susceptibilities are then simultaneously determined for all four materials from a single set of SHG and THG images. As a result, the effective bulklike second- and third-order nonlinear susceptibilities of all four materials are directly comparable. The excitation light source in our experiments is a mode-locked erbium-doped fiber laser with 1560 nm center wavelength. Thus, the resulting SHG and THG signals lie in the visible-to-near-infrared range. Additionally, this provides information about $\chi^{(2)}$ and $\chi^{(3)}$ at 1560 nm, which is important for telecommunication applications. Moreover, the NLO responses of all four TMDs under consideration are examined with linear and elliptical polarization in this work. Finally, we theoretically calculate their second- and third-order nonlinear susceptibilities through a perturbative expansion of the two-band $\mathbf{k}\cdot\mathbf{p}$ Hamiltonian for such media, including the effect of the exciton resonance. These theoretical results are in qualitative agreement with measurements.

II. EXPERIMENTAL STUDY

In our experiments, micromechanically exfoliated samples of MoS_2, $MoSe_2$, WS_2, and WSe_2 were transferred onto a Si/SiO_2 (285 nm) substrate, close to each other. The sample fabrication process is similar to that reported in Refs. [37,38] (fabrication details in the Supplemental Material [39]). The transferred flakes were then identified and characterized through optical contrast, Raman spectroscopy, and photoluminescence (PL) measurements. The Raman peak separation can be used to extract the layer thickness [40,41]. Details of these measurements are provided in the Supplemental Material [39]. Figure 1 shows an optical image of the fabricated sample. The ML flake of WS_2 is shown as an inset because it is placed slightly farther away from the other materials, outside the image field of view. Additionally, graphene monolayers were exfoliated on a similar substrate for comparison. Strain and doping can have a significant effect on the (nonlinear) optical properties of 2D materials. The possible presence of strain is excluded based on the measured Raman spectra. For example, in Ref. [42], it was shown that the E_{2g} peak in MoS_2 shifts by 4.5 cm^{-1} per percent strain and splits into two separate subpeaks already at 0.5% strain, which we do not see in any of our measurements (see Figs. 2 and 3 in the SM). Furthermore, the 2D materials are obtained from undoped bulk crystals and, since we are using a dry-transfer technique, the samples are not chemically doped. This is different from other transfer methods, in which the chemicals used during the transfer process might introduce the doping effect. The doping level can also be modified due to the substrate. For example, SiO_2 can have a high degree of charge impurities at the surface which can lead to an altered doping level of the sample [43]. The effect of doping on the nonlinear optical response of 2D materials is still largely unexplored. However,

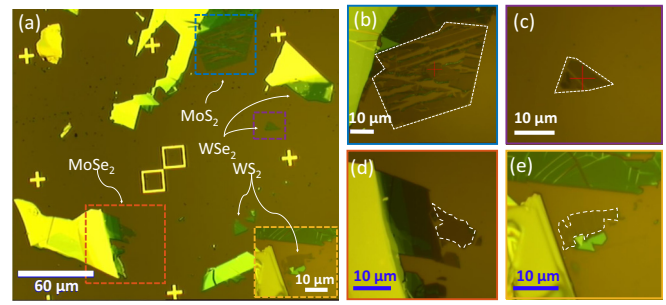

FIG. 1. (a) Optical image of four different TMDs positioned close to each other. Zoomed optical images of areas marked in (a) with colored rectangles for (b) MoS_2, (c) WSe_2, (d) $MoSe_2$, and (e) WS_2. White dashed contours in (b)–(e) indicate the monolayer areas.

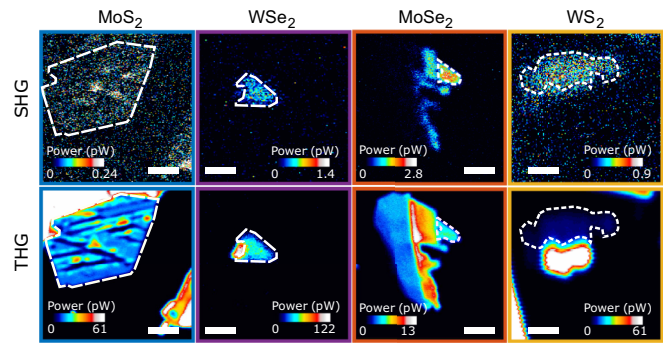

FIG. 2. SHG (top) and THG (bottom) images from the areas marked with colored dashed rectangles in the optical image of Fig. 1(a). Blue, MoS_2; purple, WSe_2; orange, $MoSe_2$; yellow, WS_2. The scale bar for MoS_2, WSe_2, and $MoSe_2$ is 10 μm, and that for WS_2 is 5 μm.

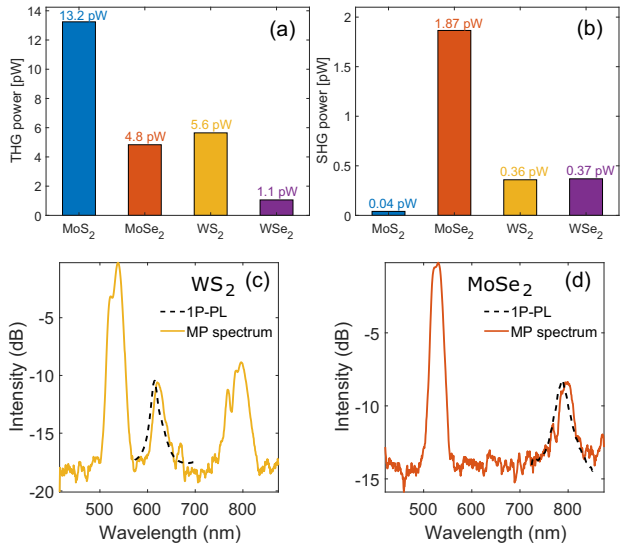

FIG. 3. Measured average powers of (a) THG and (b) SHG from monolayers of all four materials with 20 mW pump power (∼2.7 kW peak power). Comparison between one-photon and multiphoton excited spectrum of (c) WS_2 and (d) $MoSe_2$. Note that the intensities of one-photon and multiphoton spectra in (c) and (d) are not to scale.

in Ref. [33] SHG from MoS_2 on SiO_2 and polymer substrates was measured. With a fundamental wavelength at 1600 nm they measured a $\chi^{(2)}$ of 6.3 pm/V on the SiO_2 substrate and 7 pm/V on the polymer substrate, suggesting that the doping from the substrate may not be substantial. As noted earlier, to best of our knowledge there are no studies on the effect of chemical- or substrate-induced doping on nonlinear optical properties of 2D materials at different wavelengths, so it is not possible to accurately assess the different contributions on the nonlinear optical responses of the four TMDs studied here. However, this is a highly interesting topic for future research.

The SHG and THG for the four materials under examination (Fig. 2) were collected using a mode-locked fiber laser with 1560 nm center wavelength. Each different area (located within a distance <150 μm from each other) possesses exfoliated TMD flakes, whose thicknesses range from one to a few atomic monolayers (see the SM for thickness determination). The small distance between the locations of the exfoliated MoS_2, $MoSe_2$, WS_2, and WSe_2 allows us to easily compare the optical nonlinearities of the different materials. As a result, this excludes the effect of substrate and varying measurement conditions on the measured susceptibilities because the recorded SHG and THG powers can be obtained from the same SHG or THG image for all materials. The locations of the nonlinear microscopy images are indicated by dashed rectangles in the optical image in Fig. 1. We observed a SHG signal and a strong THG signal from all four TMDs, within a single image, of which Fig. 2 selects zoomed regions.

The reported values of SHG and THG signals are all obtained from the locations in which each TMD flake is a single layer thick. Prior to comparison, however, in order to prove that the measured signals at 780 and 520 nm in fact originate from SHG and THG, respectively, power-dependent nonlinear microscopy measurements were performed for all four materials (see SM, Fig. 10). These measurements clearly indicate P^2 (SHG) and P^3 (THG) dependencies, with the incident light power P. Note that this is the first time that THG can be observed in WSe_2, $MoSe_2$, and WS_2. The average powers of SHG and THG from monolayers of all four materials are shown in Figs. 3(a) and 3(b). Normally at a reasonable pump power, THG intensity is expected to be lower than SHG intensity, due to the weaker intrinsic response of the higher-order nonlinear processes [44]. It is surprising that THG is clearly stronger than SHG in all four TMDs at such a low average pump power (e.g., Figs. 3(c) and 3(d)). The same effect was recently observed in MoS_2, and explained with the contribution of trigonal warping to the second-order response [28]. With low incident photon energies (0.8 eV here and in Ref. [28]), SHG is weaker than expected for MoS_2 due to near-isotropic bands contributing to the SHG signal. Only trigonal warping breaks the approximate rotational invariance of the monolayer MoS_2 band structure, causing the SHG emission [28]. More insight into the possible effects of trigonal warping or other causes (e.g., excitons) leading to the large observed ratio between THG and SHG could be obtained by measuring the SHG and THG from all four materials with a large range of excitation wavelengths. Note that the SHG intensity from $MoSe_2$ is lower than the intensity of THG, even though the SHG is on resonance with the A exciton [17,21,24,45,46]. Furthermore, we observe clearly distinct THG and SHG signals for different TMDs. For instance, THG is largest from MoS_2 and smallest from WSe_2. In contrast, SHG from $MoSe_2$ is ∼4–40 times larger than that from the other materials. This can be attributed to resonant enhancement in $MoSe_2$ because the energy of the A exciton in this material (∼1.57 eV, 790 nm [47]) matches well with the wavelength (780 nm, 1.59 eV). In fact, the spectral overlap of excitonic PL and SHG is well visualized in Fig. 3(d), which shows the PL spectrum measured with 532 nm excitation, and the multiphoton (MP) excited spectrum [containing SHG, THG, and two-photon excited luminescence (2PL)] for $MoSe_2$.

We note that the MP excited spectrum of WS_2 also shows a peak at ∼615 nm (2.01 eV), corresponding to the location of the PL peak [Fig. 3(c)]. Thus, we attribute this peak to three-photon excited luminescence (3PL) from monolayer WS_2. Since 3PL ensues from a fifth-order NLO process [48], the probability of 3PL occurrence is very low. Interestingly, the intensity of 3PL is in the same range as the intensity of SHG. 2PL spectroscopy has been used to study the excitons in TMD monolayers because with 2PL it is possible to probe dark exciton states, which are forbidden by selection rules for one-photon excitation [49,50]. Graphene and MoS_2 quantum dots have been used as 2PL probes in cellular and deep-tissue imaging [51,52]. However, 3PL can provide better spatial resolution [53] and enable alternative excitation wavelengths; thus WS_2 might find new applications in biomedical imaging. Furthermore, 3PL spectroscopy might provide an alternative method for probing excitonic features in monolayer TMDs.

We estimate the effective second- and third-order nonlinear susceptibilities $|\chi^{(2)}_{\text{eff}}|$ and $|\chi^{(3)}_{\text{eff}}|$ of all TMDs from the measured average SHG and THG powers. The sheet susceptibility

TABLE I. Theoretical and experimental $|\chi^{(2)}|$ and $|\chi^{(3)}|$ values of different TMD materials.

	$\lvert\chi^{(2)}\rvert$ (10^{-12} m/V)		$\lvert\chi^{(3)}\rvert$ (10^{-19} m^2/V^2)	
Material	Theor.	Expt.	Theor.	Expt.
MoS_2	420	5.4	17	3.6
$MoSe_2$	810	37.0	29	2.2
WS_2	424	16.2	24	2.4
WSe_2	311	16.5	25	1.0

values, $\chi_s^{(n)}$, are estimated with the methods described in Ref. [29], by fitting the measured average powers to the following two equations:

$$P_{\mathrm{SHG}} = \frac{16\sqrt{2}S\left|\chi_s^{(2)}\right|^2\omega^2}{c^3\varepsilon_0 f\pi r^2\tau(1+n_2)^6}P_1^2, \tag{1}$$

$$P_{\mathrm{THG}} = \frac{64\sqrt{3}S^2\left|\chi_s^{(3)}\right|^2\omega^2}{c^4\varepsilon_0^2(f\pi r^2\tau)^2(1+n_2)^8}P_1^3, \tag{2}$$

where $S = 0.94$ is the shape factor for Gaussian pulses, τ is the temporal pulse width, P_1 is the incident average power of the pump beam, f is the repetition rate, n_2 is the refractive index of the substrate at the pump wavelength, and ω is the angular frequency of the pump. The effective bulklike second-order susceptibility of TMDs is obtained from the sheet susceptibilities as

$$\left|\chi_{\mathrm{eff}}^{(n)}\right| = \frac{\left|\chi_s^{(n)}\right|}{t},$$

where t is the thickness of the TMD monolayer, ~0.65 nm.

The $|\chi_{\mathrm{eff}}^{(2)}|$ and $|\chi_{\mathrm{eff}}^{(3)}|$ values measured from different TMDs in this work are presented in Table I and Fig. 4. Furthermore, $|\chi_{\mathrm{eff}}^{(2)}|$ and $|\chi_{\mathrm{eff}}^{(3)}|$ values for various monolayer TMDs from other measurements reported in the literature are presented in Table 1 in the SM.

Note that $|\chi_{\mathrm{eff}}^{(2)}|$ values obtained in this work lie in the range between 5.4×10^{-12} and 37.0×10^{-12} m V^{-1} for all ML-TMDs. These values are in good agreement with those reported in the literature for TMDs when they have been measured with excitation wavelength in the IR region. For instance, the literature values of $|\chi_{\mathrm{eff}}^{(2)}|$ for MoS_2 [28,29,54,55] range between 2.2×10^{-12} and 29×10^{-12} m V^{-1} and thus match reasonably well with the value of 5.4×10^{-12} m V^{-1} obtained in this work for 1560 nm excitation.

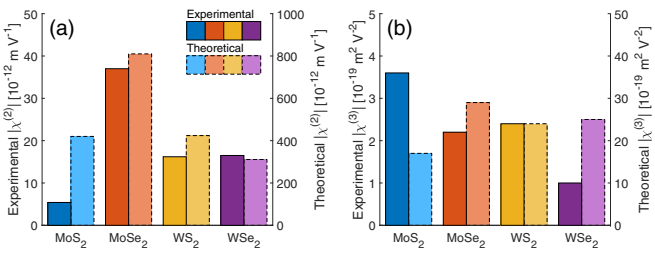

FIG. 4. Comparison of experimental and theoretical (a) $|\chi^{(2)}|$ and (b) $|\chi^{(3)}|$ of four TMDs at 1560 nm excitation.

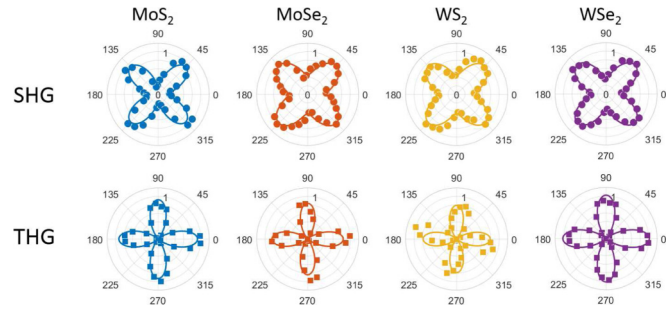

FIG. 5. Polar plots of normalized SHG and THG signals as a function of the quarter-wave plate (QWP) angle. The angle is defined between the polarization of the incident laser and the fast axis of the QWP.

We note that the $|\chi_{\mathrm{eff}}^{(2)}|$ for MoS_2 is two orders of magnitude smaller than what has been measured with 800 nm excitation [8,21]. On the other hand, $|\chi_{\mathrm{eff}}^{(3)}|$ values for all characterized TMDs are in the range between 1.0×10^{-19} and 3.6×10^{-19} m^2 V^{-2}. We also find excellent agreement with previous literature values for $|\chi_{\mathrm{eff}}^{(3)}|$ when measured at a similar wavelength. For instance, the magnitude of the $|\chi_{\mathrm{eff}}^{(3)}|$ values for MoS_2 is of the order of 1×10^{-19} m^2 V^{-2} (see Refs. [27–29]) and therefore in the same range as the value of 3.6×10^{-19} m^2 V^{-2} reported in this work. The effect of the substrate should also be taken into account when comparing the values. In Ref. [29] the bulklike $|\chi^{(2)}|$ and $|\chi^{(3)}|$ of MoS_2 were measured on glass and on Si/SiO_2 substrates. It was found that the $|\chi^{(2)}|$ did not exhibit significant change but the $|\chi^{(3)}|$ was enhanced by a factor of 5 due to the interferometric effect caused by the multilayer structure. However, this does not affect the comparison between the four materials, as the effect hold for all of them, in this experiment.

The intensities of SHG and THG depend strongly on the polarization state of the pump and the crystallographic orientation of the sample [8,28,29,31]. In order to explore this effect, we have measured SHG and THG from all four materials using elliptically polarized excitation light with varying degree of ellipticity. Figure 5 show the measured SHG and THG intensities as a function of incident light polarization state. As shown in this figure, the THG signal is strongest for linearly polarized excitation light and smallest for circular polarization. In contrast, the SHG signal is strongest for circularly polarized excitation light and smallest for linearly polarized excitation light. Because all four materials belong to the point group D_{3h}^1, similar results are obtained for the other crystals, $MoSe_2$, WS_2, and WSe_2. This paves the way for tailoring the nonlinear optical properties of 2D materials arranged in heterostructures.

III. THEORETICAL ANALYSIS AND COMPARISON TO EXPERIMENTAL VALUES

In order to obtain further insight into the origin of the NLO behavior under study, we theoretically calculate the second- and third-order nonlinear susceptibilities of all four materials

through a perturbative expansion of the two-band $\mathbf{k}\cdot\mathbf{p}$ Hamiltonian for such media [56] under the minimum coupling prescription $\boldsymbol{\pi} = \mathbf{p} + e\mathbf{A}(t)$, where e is the electron charge, $\mathbf{A}(t)$ is the potential vector of the impinging light beam, and $\mathbf{p}$ and $\boldsymbol{\pi}$ are the electron momentum and quasimomentum, respectively.

The two-band $\mathbf{k}\cdot\mathbf{p}$ Hamiltonian is obtained by fitting the valence and conduction bands of the tight-binding Hamiltonian reported in the literature [56] that account for both nondegenerate valleys and spin-orbit coupling. The effect of the exciton resonance on the nonlinear parameters of $MoSe_2$ is taken into account by introducing an effective exciton energy level in the single-particle Hamiltonian after fitting the linear conductivity with fully numerical Bethe-Salpeter calculations [57]. Results are presented in Table I and compared with experiment in Fig. 4, while technical details of the calculations are provided in the SM [39]. These theoretical calculations predict a generally higher value of the nonlinear coefficients, roughly one order of magnitude larger than the corresponding measured quantities. Such calculations confirm that $MoSe_2$ is the ML-TMD with highest $|\chi^{(2)}|$ nonlinear coefficient, although the relative difference with respect to other TMDs is not as marked as in experiments. A mismatch of relative values across different materials also appears in the $\chi^{(3)}$ calculations, which predict that $MoSe_2$ has the highest $|\chi^{(3)}|$, in contrast to experiment, in which MoS_2 exhibits the highest third-order nonlinearity. We envisage that this may be due to the effect of the substrate on electron many-body dynamics, which deserves further attention. In addition, the substrate is expected to induce subtle modifications on the band structure. While the linear response of the 2D layers under consideration remains unaffected because it mainly depends on the energy band gap, the NLO response originates in the anharmonicity of the bands and thus it is much more sensitive to small modifications in the band structure arising from the interaction of ML-TMDs with the substrate. Comparison with our experimental results provides an indication of the trends when examining different materials and also on the orders of the magnitude of the effects. Nevertheless, future theoretical efforts beyond the scope of this work are required to obtain a good quantitative agreement. We envisage that, in order to improve predictions, future theoretical efforts should include more electronic bands, account for the interaction of the considered two-dimensional media with the substrate (which modifies the electronic band structure), and ultimately rely on first-principle simulations to fully describe the nonlinear exciton dynamics beyond the effective exciton band model used in our calculations (see the SM [39]).

IV. CONCLUSIONS

In summary, in this work we demonstrate third-harmonic generation in WSe_2, $MoSe_2$, and WS_2 and three-photon photoluminescence in TMDs. We also report the direct comparison of second- and third-order optical nonlinearities in MoS_2, $MoSe_2$, WS_2, and WSe_2. The $\chi^{(2)}$ of $MoSe_2$ is found to be approximately two to six times larger than that of the other TMDs examined here. We attribute this effect to resonant enhancement of SHG in $MoSe_2$. The third-order nonlinear susceptibility $\chi^{(3)}$ of all four materials is found to be comparable to that of graphene, with the largest value $|\chi^{(3)}_{\text{eff}}| = 3.6\times10^{-19}$ $\text{m}^2\,\text{V}^{-2}$ observed for MoS_2. We obtain further insight into the NLO properties by theoretically calculating the second- and third-order nonlinear susceptibilities of all four materials, in qualitative agreement with measurements.

Furthermore, the effect of the degree of elliptical polarization of the incident light on the SHG and THG signals was examined and we found that the SHG signal was enhanced and the THG one was completely suppressed with circular polarization. Experimental results fit very well with expected values based on previously reported expressions derived from the crystal symmetry for MoS_2. The results presented here provide valuable information about the nonlinear properties of the different TMDs for the design of devices based on 2D materials and their heterostructures in a wide range of applications, such as on-chip light sources and all-optical signal processing.

ACKNOWLEDGMENTS

We acknowledge funding from the Academy of Finland (Grants No. 276376, No. 284548, No. 295777, No. 298297, No. 304666, No. 312551, No. 312297, and No. 314810), TEKES (NP-Nano, OPEC), the Nokia Foundation, Tekniikan edistämissäätiö (TES), Aalto Centre of Quantum Engineering, the China Scholarship Council, Spanish MINECO (MAT2017-88492-R and SEV2015-0522), the European Commission (REA Grant No. 631610, Graphene Flagship 696656) and AGAUR (FI_B-00492-2015 and 2017-SGR-1651). We acknowledge the provision of facilities and technical support by Aalto University at Micronova Nanofabrication Centre.

[1] A. C. Ferrari, F. Bonaccorso, V. Fal'ko, K. S. Novoselov, S. Roche, P. Boggild, S. Borini, F. H. Koppens, V. Palermo, N. Pugno, J. A. Garrido, R. Sordan, A. Bianco, L. Ballerini, M. Prato, E. Lidorikis, J. Kivioja, C. Marinelli, T. Ryhanen, A. Morpurgo, J. N. Coleman, V. Nicolosi, L. Colombo, A. Fert, M. Garcia-Hernandez, A. Bachtold, G. F. Schneider, F. Guinea, C. Dekker, M. Barbone, Z. Sun, C. Galiotis, A. N. Grigorenko, G. Konstantatos, A. Kis, M. Katsnelson, L. Vandersypen, A. Loiseau, V. Morandi, D. Neumaier, E. Treossi, V. Pellegrini, M. Polini, A. Tredicucci, G. M. Williams, B. H. Hong, J. H. Ahn, J. M. Kim, H. Zirath, B. J. van Wees, H. van der Zant, L. Occhipinti, A. Di Matteo, I. A. Kinloch, T. Seyller, E. Quesnel, X. Feng, K. Teo, N. Rupesinghe, P. Hakonen, S. R. Neil, Q. Tannock, T. Lofwander, and J. Kinaret, Nanoscale **7**, 4598 (2015).

[2] F. Bonaccorso, Z. Sun, T. Hasan, and A. C. Ferrari, Nat. Photonics **4**, 611 (2010).

[3] K. F. Mak, C. Lee, J. Hone, J. Shan, and T. F. Heinz, Phys. Rev. Lett. **105**, 136805 (2010).

[4] A. Splendiani, L. Sun, Y. Zhang, T. Li, J. Kim, C.-Y. Chim, G. Galli, and F. Wang, Nano Lett. **10**, 1271 (2010).

[5] Q. H. Wang, K. Kalantar-Zadeh, A. Kis, J. N. Coleman, and M. S. Strano, Nat. Nanotechnol. **7**, 699 (2012).

[6] W. Jin, P.-C. Yeh, N. Zaki, D. Zhang, J. T. Sadowski, A. Al-Mahboob, A. M. van Der Zande, D. A. Chenet, J. I. Dadap, I. P. Herman *et al.*, Phys. Rev. Lett. **111**, 106801 (2013).

[7] Z. Sun, A. Martinez, and F. Wang, Nat. Photonics **10**, 227 (2016).

[8] Y. Li, Y. Rao, K. F. Mak, Y. You, S. Wang, C. R. Dean, and T. F. Heinz, Nano Lett. **13**, 3329 (2013).

[9] A. Autere, H. Jussila, Y. Dai, Y. Wang, H. Lipsanen, and Z. Sun, Adv. Mater. **30**, 1705963 (2018).

[10] T. Gu, N. Petrone, J. F. McMillan, A. van der Zander, M. Yu, G. Q. Lo, D. L. Kwong, J. Hone, and C. W. Wong, Nat. Photonics **6**, 554 (2012).

[11] E. Hendry, P. J. Hale, J. Moger, A. K. Savchenko, and S. A. Mikhailov, Phys. Rev. Lett. **105**, 097401 (2010).

[12] S. Li, Y.-C. Lin, W. Zhao, J. Wu, Z. Wang, Z. Hu, Y. Shen, D.-M. Tang, J. Wang, Q. Zhang, H. Zhu, L. Chu, W. Zhao, C. Liu, Z. Sun, T. Taniguchi, M. Osada, W. Chen, Q.-H. Xu, A. T. S. Wee, K. Suenaga, F. Ding, and G. Eda, Nat. Mater. **17**, 535 (2018).

[13] X. Yang, Z. Sun, T. Low, H. Hu, X. Guo, F. J. García de Abajo, P. Avouris, and Q. Dai, Adv. Mater. **30**, 1704896 (2018).

[14] Z. Sun, Nat. Photonics **12**, 383 (2018).

[15] H. Chen, V. Corboliou, A. S. Solntsev, D.-Y. Choi, M. A. Vincenti, D. de Ceglia, C. de Angelis, Y. Lu, and D. N. Neshev, Light Sci. Appl. **6**, e17060 (2017).

[16] T. K. Fryett, K. L. Seyler, J. Zheng, C.-H. Liu, X. Xu, and A. Majumdar, 2D Mater. **4**, 015031 (2017).

[17] G. Wang, S. Zhang, X. Zhang, L. Zhang, Y. Cheng, D. Fox, H. Zhang, J. N. Coleman, W. J. Blau, and J. Wang, Photonics Res. **3**, A51 (2015).

[18] A. Autere, C. Ryder, A. Saynatjoki, L. Karvonen, B. Amirsolaimani, R. Norwood, N. Peyghambarian, K. Kieu, H. Lipsanen, M. Hersam, and Z. Sun, J. Phys. Chem. Lett. **8**, 1343 (2017).

[19] J. Liang, J. Zhang, Z. Li, H. Hong, J. Wang, Z. Zhang, X. Zhou, R. Qiao, J. Xu, P. Gao, Z. Liu, Z. Liu, Z. Sun, S. Meng, K. Liu, and D. Yu, Nano Lett. **17**, 7539 (2017).

[20] X. Zhou, J. Cheng, Y. Zhou, T. Cao, H. Hong, Z. Liao, S. Wu, H. Peng, J. Xu, K. Liu, and D. Yu, J. Am. Chem. Soc. **137**, 7994 (2015).

[21] L. M. Malard, T. V. Alencar, Ana Paula M. Barboza, K. F. Mak, and A. M. de Paula, Phys. Rev. B **87**, 201401 (2013).

[22] N. Kumar, S. Najmaei, Q. Cui, F. Ceballos, P. M. Ajayan, J. Lou, and H. Zhao, Phys. Rev. B **87**, 161403 (2013).

[23] K.-I. Lin, Y.-H. Ho, S.-B. Liu, J.-J. Ciou, B.-T. Huang, C. Chen, H.-C. Chang, C.-L. Tu, and C.-H. Chen, Nano Lett. **18**, 793 (2018).

[24] C. T. Le, D. J. Clark, F. Ullah, V. Senthilkumar, J. I. Jang, Y. Sim, M.-J. Seong, K.-H. Chung, H. Park, and Y. S. Kim, Ann. Phys. **528**, 551 (2016).

[25] C. Janisch, Y. Wang, D. Ma, N. Mehta, A. L. Elías, N. Perea-López, M. Terrones, V. Crespi, and Z. Liu, Sci. Rep. **4**, 5530 (2014).

[26] H. Zeng, G.-B. Liu, J. Dai, Y. Yan, B. Zhu, R. He, L. Xie, S. Xu, X. Chen, and W. Yao, Sci. Rep. **3**, 1608 (2013).

[27] R. Wang, H.-C. Chien, J. Kumar, N. Kumar, H.-Y. Chiu, and H. Zhao, ACS Appl. Mater. Interfaces **6**, 314 (2013).

[28] A. Säynätjoki, L. Karvonen, H. Rostami, A. Autere, S. Mehravar, A. Lombardo, R. Norwood, T. Hasan, N. Peyghambarian, H. Lipsanen, K. Kieu, A. Ferrari, M. Polini, and Z. Sun, Nat. Commun. **8**, 893 (2017).

[29] R. I. Woodward, R. T. Murray, C. F. Phelan, R. E. P. de Oliveira, T. H. Runcorn, E. J. R. Kelleher, S. Li, E. C. de Oliveira, G. J. M. Fechine, G. Eda, and C. J. S. de Matos, 2D Mater. **4**, 011006 (2017).

[30] L. Karvonen, A. Säynätjoki, M. J. Huttunen, A. Autere, B. Amirsolaimani, S. Li, R. A. Norwood, N. Peyghambarian, H. Lipsanen, G. Eda, K. Kieu, and Z. Sun, Nat. Commun. **8**, 15714 (2017).

[31] H. Liu, Y. Li, Y. S. You, S. Ghimire, T. F. Heinz, and D. A. Reis, Nat. Phys. **13**, 262 (2017).

[32] M. Merano, Opt. Lett. **41**, 187 (2016).

[33] D. J. Clark, C. T. Le, V. Senthilkumar, F. Ullah, H.-Y. Cho, Y. Sim, M.-J. Seong, K.-H. Chung, Y. S. Kim, and J. I. Jang, Appl. Phys. Lett. **107**, 131113 (2015).

[34] X. Miao, N. Xuan, Q. Liu, W. Wu, H. Liu, Z. Sun, and M. Ji, ACS Appl. Mater. Interfaces **9**, 34448 (2017).

[35] C. Torres-Torres, N. Perea-López, A. L. Elías, H. R. Gutiérrez, D. A. Cullen, A. Berkdemir, F. López-Urías, H. Terrones, and M. Terrones, 2D Mater. **3**, 021005 (2016).

[36] W. Wang, Y. Wu, Q. Wu, J. Hua, and J. Zhao, Sci. Rep. **6**, 22072 (2016).

[37] A. Castellanos-Gomez, M. Buscema, R. Molenaar, V. Singh, L. Janssen, H. S van der Zant, and G. A Steele, 2D Mater. **1**, 011002 (2014).

[38] D. Li, H. Jussila, L. Karvonen, G. Ye, H. Lipsanen, X. Chen, and Z. Sun, Sci. Rep. **5**, 15899 (2015).

[39] See Supplemental Material at http://link.aps.org/supplemental/10.1103/PhysRevB.98.115426 for a more detailed description of the experimental methods, including Raman and photoluminescence characterization, and the theoretical calculations.

[40] H. Li, Q. Zhang, C. C. R. Yap, B. K. Tay, T. H. T. Edwin, A. Olivier, and D. Baillargeat, Adv. Funct. Mater. **22**, 1385 (2012).

[41] A. Berkdemir, H. R. Gutiérrez, A. R. Botello-Méndez, N. Perea-López, A. L. Elías, C.-I. Chia, B. Wang, V. H. Wang, F. López-Urías, J.-C. Charlier, H. Terrones, and M. Terrones, Sci. Rep. **3**, 01755 (2013).

[42] H. J. Conley, B. Wang, J. I. Ziegler, R. F. Haglund, Jr., S. T. Pantelides, and K. I. Bolotin, Nano Lett. **13**, 3626 (2013).

[43] M. Buscema, G. A. Steele, H. S. van der Zant, and A. Castellanos-Gomez, Nano Res. **7**, 561 (2014).

[44] R. W. Boyd, *Nonlinear Optics* (Academic Press, New York, 2003).

[45] K. L. Seyler, J. R. Schaibley, P. Gong, P. Rivera, A. M. Jones, S. Wu, J. Yan, D. G. Mandrus, W. Yao, and X. Xu, Nat. Nanotechnol. **10**, 407 (2015).

[46] G. Wang, I. C. Gerber, L. Lagarde, A. Balocchi, M. Vidal, T. Amand, X. Marie, D. G. Mandrus, and B. Urbaszek, 2D Mater. **2**, 045005 (2015).

[47] P. Tonndorf, R. Schmidt, P. Böttger, X. Zhang, J. Börner, A. Liebig, M. Albrecht, C. Kloc, O. Gordan, D. R. T. Zahn, S. M. de Vasconcellos, and R. Bratschitsch, Opt. Express **21**, 4908 (2013).

[48] J. Qian, Z. Zhu, A. Qin, W. Qin, L. Chu, F. Cai, H. Zhang, Q. Wu, R. Hu, B. Z. Tang, and S. He, Adv. Mater. **27**, 2332 (2015).

[49] Z. Ye, T. Cao, K. O'Brien, H. Zhu, X. Yin, Y. Wang, S. G. Louie, and X. Zhang, Nature (London) **513**, 214 (2014).

[50] K. He, N. Kumar, L. Zhao, Z. Wang, K. F. Mak, H. Zhao, and J. Shan, Phys. Rev. Lett. **113**, 026803 (2014).

[51] Q. Liu, B. Guo, Z. Rao, B. Zhang, and J. R. Gong, Nano Lett. **13**, 2436 (2013).

[52] W. Dai, H. Dong, B. Fugetsu, Y. Cao, H. Lu, X. Ma, and X. Zhang, Small **11**, 4158 (2015).

[53] J. H. Yu, S.-H. Kwon, Z. Petrasek, O. K. Park, S. W. Jun, K. Shin, M. Choi, Y. I. Park, K. Park, H. B. Na, N. Lee, D. W. Lee, J. H. Kim, P. Schwille, and T. Hyeon, Nat. Mater. **12**, 359 (2013).

[54] C. T. Le, D. J. Clark, F. Ullah, J. I. Jang, V. Senthilkumar, Y. Sim, M.-J. Seong, K.-H. Chung, J. W. Kim, S. Park, S. H. Rhim, G. Kim, and Y. S. Kim, ACS Photonics **4**, 38 (2017).

[55] D. J. Clark, V. Senthilkumar, C. T. Le, D. L. Weerawarne, B. Shim, J. I. Jang, J. H. Shim, J. Cho, Y. Sim, M.-J. Seong, S. H. Rhim, A. J. Freeman, K.-H. Chung, and Y. S. Kim, Phys. Rev. B **90**, 121409 (2014).

[56] G.-B. Liu, W.-Y. Shan, Y. Yao, W. Yao, and D. Xiao, Phys. Rev. B **88**, 085433 (2013).

[57] A. Marini, C. Hogan, M. Grunig, and D. Varsano, Comput. Phys. Commun. **180**, 1392 (2009).

Supplemental Material for Optical harmonic generation in monolayer group-VI transition metal dichalcogenides

Anton Autere,[1] Henri Jussila,[1] Andrea Marini,[2] J. R. M. Saavedra,[2] Yunyun Dai,[1] Antti Säynätjoki,[1,3] Lasse Karvonen,[1] He Yang,[1] Babak Amirsolaimani,[4] Robert A. Norwood,[4] N. Peyghambarian,[4,3,1] Harri Lipsanen,[1] Khanh Kieu,[4] F. Javier García de Abajo,[2,5] and Zhipei Sun[1]

[1] *Department of Electronics and Nanoengineering, Aalto University, P.O.Box 13500, FI-00076 Aalto, Finland*
[2] *ICFO-Institut de Ciències Fotòniques, The Barcelona Institute of Science and Technology, 08860 Castelldefels, Barcelona, Spain*
[3] *Institute of Photonics, University of Eastern Finland, Yliopistokatu 7, FI-80101 Joensuu, Finland*
[4] *College of Optical Sciences, University of Arizona, 1630 E. University Boulevard, Tucson, Arizona 85721, USA*
[5] *ICREA-Institució Catalana de Recerca i Estudis Avançats, Passeig Lluís Companys 23, 08010 Barcelona, Spain*

METHODS

Sample Fabrication. The sample fabrication process used in this work is similar to that reported in Refs. 1 and 2. In brief, MoS_2, $MoSe_2$, WS_2 and WSe_2 flakes (from *2d Semiconductors Inc.*) were micromechanically exfoliated directly onto a viscoelastic polydimethylsiloxane (PDMS) stamp. Then, an optical microscope was used to identify thin flakes on the PDMS stamp. The selected flakes were pressed against the substrate (285 nm thick SiO_2 layer on silicon substrate) with a micromanipulator. Due to the viscoelastic properties of PDMS, the exfoliated flakes adhere to the target substrate when the PDMS stamp is gently lifted off.

Nonlinear Microscopy. During measurements, the laser beam was scanned with a 2D galvo-mirror and focused on the sample with a 20× microscope objective. The measurement setup was similar to the one used in Ref. 3. The SHG and THG signals were collected with the same objective lens and separated with a 562 nm dichroic mirror. Narrow-band bandpass filters were placed in front of two photo-multiplier tubes (PMTs), so that only SHG and THG were detected. The center wavelength of the excitation light was ~ 1560 nm, the repetition rate was 50 MHz, and the pulse duration was 150 fs. The maximum average power on the sample was 36 mW, which corresponds to a maximum peak power of 4.8 kW. The spot size on the sample, measured with the nonlinear razorblade method, was ~ 1.85 μm. For elliptical polarization measurements, a quarter-wave plate was placed before the galvo mirror.

Raman Scattering and PL Measurements. Raman and PL spectra were measured using a confocal Raman microscope (Witec alpha 300 R) equipped with a frequency-doubled Nd:YAG green laser ($\lambda = 532$ nm). Raman and PL mapping measurements were performed with the same tool by scanning the laser over the sample and recording the Raman and PL spectra as a function of location.

TABLE OF $\chi^{(2)}$ AND $\chi^{(3)}$ VALUES REPORTED IN LITERATURE

TABLE I. Bulk-like $|\chi^{(2)}_{\text{eff}}|$ and $|\chi^{(3)}_{\text{eff}}|$ values of different TMD materials measured in this work and comparison to the values reported in literature.

Material	$\chi^{(2)}_{\text{eff}}$ $\left[\frac{\text{m}}{\text{V}}\right]$	$\chi^{(3)}_{\text{eff}}$ $\left[\frac{\text{m}^2}{\text{V}^2}\right]$	λ_ω	Ref.
Graphene	–	1.03×10^{-19}	1560 nm	This work
MoS_2	5.4×10^{-12}	3.6×10^{-19}	1560 nm	This work
$MoSe_2$	37.0×10^{-12}	2.2×10^{-19}	1560 nm	This work
WS_2	16.2×10^{-12}	2.4×10^{-19}	1560 nm	This work
WSe_2	16.5×10^{-12}	1.0×10^{-19}	1560 nm	This work
MoS_2	5×10^{-12}		1560 nm	4
MoS_2	29×10^{-12}	$\sim 10^{-19}$	1560 nm	5
MoS_2	$\sim 2 \times 10^{-12}$	1.2×10^{-19}	1560 nm	6
MoS_2	2.2×10^{-12}	5.2×10^{-19}	1560 nm	3
MoS_2	5×10^{-12}		1560 nm	7
WSe_2	15×10^{-12}		1550 nm	8
$MoSe_2$	25×10^{-12}		1560 nm	4
MoS_2*		$\sim 10^{-19}$	1700 nm	9
$MoSe_2$	$(10 - 15) \times 10^{-12}$		1560 nm	10
MoS_2	4.3×10^{-10}		1600 nm	11
WS_2	9×10^{-9}		832 nm	12
WSe_2	10×10^{-9}		816 nm	13
MoS_2	321×10^{-12}		810 nm	14
MoS_2	123×10^{-12}		885 nm	15
MoS_2	$\sim 10^{-7}$		810 nm	16
WS_2†		2.61×10^{-17}		17
$MoSe_2$‡		1.53×10^{-17}		18

*Obtained from ~ 5 nm thick flakes

†Data obtained using two-wave mixing method

‡Data obtained using self-phase modulation method

SHG AND THG IMAGES OF ALL FOUR MATERIALS

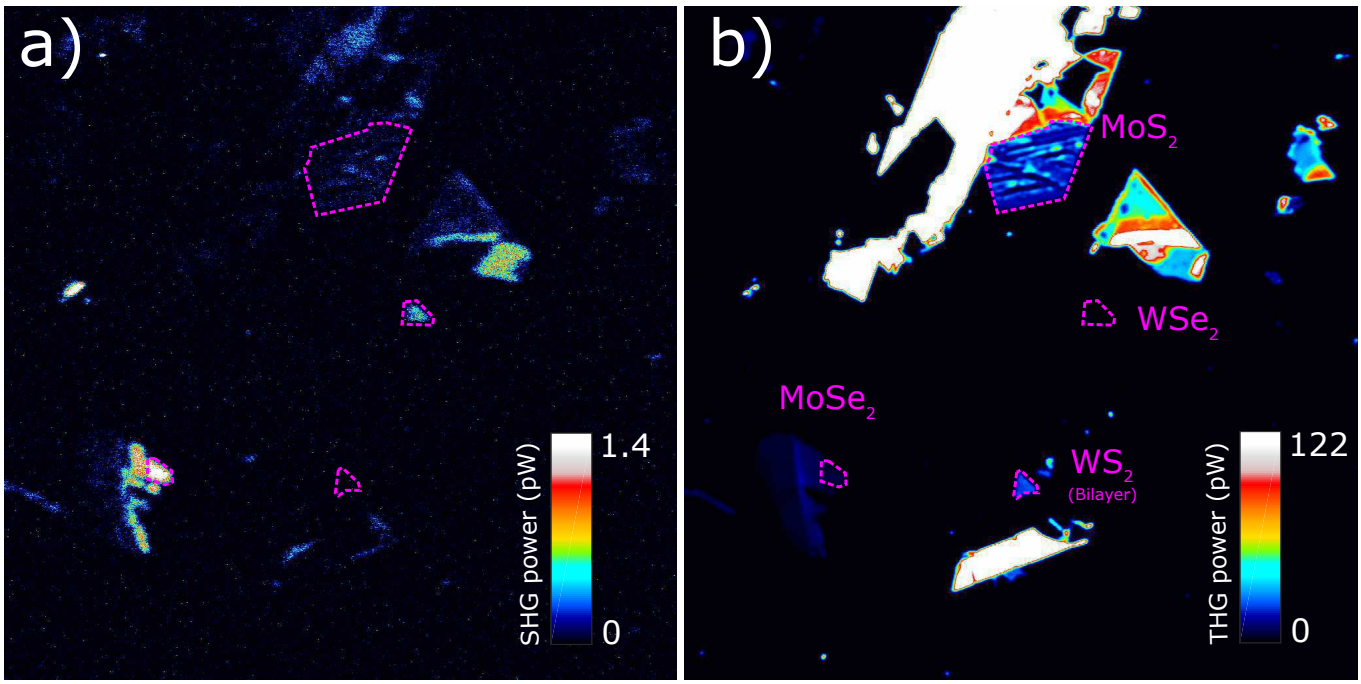

FIG. 1. SHG (a) and THG (b) images displaying all four materials in one image.

RAMAN AND PHOTOLUMINESCENCE MEASUREMENTS

MoS_2

Layer thickness identification to MoS_2 flake discussed in the main document was performed with μ-Raman and μ-photoluminescence (μPL) measurements. Fig. 2 presents an optical image of the flake in addition to the Raman spectra measured from few different locations of the flake. The optical contrast from MoS_2 flake differs between different locations, which suggests variations within the flake thickness. Note that the transfer process of this flake (which usually operates with a yield of $\sim$ 90% after the suitable flake has been found) was not perfectly successful, creating well resolvable ruptures in the flake.

Three areas (marked with letters A, B and C) were characterized more thoroughly. Raman spectrum measured from these locations is shown in Fig. 2(b). Two Raman modes are observed in all spectra close to the wavenumbers of $\sim$385 cm^{-1} and $\sim$409 cm^{-1}. These Raman peaks originate from the in-plane E^1_{2g} and out-of-plane A_{1g} vibration modes, respectively[19]. It has been reported that the separation between the Raman peaks decreases with decreasing layer thickness thereby providing a good measure for the flake thickness. The Raman peak separation in bulk MoS_2 is $\sim$26 cm^{-1}. In general, a peak separation of $\sim$19 cm^{-1} is considered a value typically measured from single layer MoS_2 flakes[20]. On the other hand, the Raman mode separation of 23.3cm^{-1} has been observed for three layer thick MoS_2 flake[20]. The Raman mode separation is calculated as 19.3 cm^{-1}, 19.7 cm^{-1}, and 23.7 cm^{-1} from the fitted Lorenzian line profiles (see the inset) in locations A, B and C, respectively. Therefore, this implies that the flake thickness in locations A and B is single layer and that the flake thickness increases to 3-5 layers in location C, as also expected based on the optical image.

Other MoS_2 flakes were characterized to obtain statistical credibility to the values reported in this work. Fig. 3 presents the optical, SHG and THG images of another MoS_2 flake in addition to the μ-Raman and μ-PL spectra measured from few different locations of the flake. This time the Raman peak separation at the locations D, E and F (marked in Fig. 3(a)) is 18.7 cm^{-1}, 18.8 cm^{-1} and 21.5 cm^{-1} suggesting that areas D-E are monolayers and area F is bilayer. In addition to the Raman measurements, also μ-PL spectra were measured from these locations to further verify the flake thickness. In fact, the observation of strong PL from the exfoliated MoS_2 flakes provides more evidence

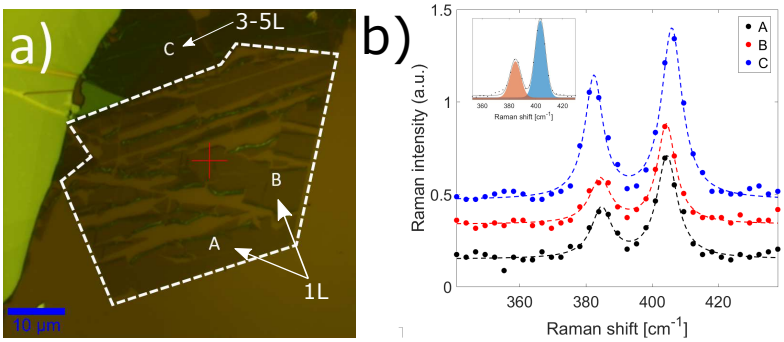

FIG. 2. Optical image (a) and Raman spectra (b) of the MoS_2 flake discussed in the main text. The inset shows fitted E^1_{2g} and A_{1g} Raman peaks.

for the flake thickness. Fig. 3(e) shows the measured μ-PL spectra. As expected, well resolvable PL is observed from all locations. The PL spectrum possesses two transitions at the wavelengths of ∼630 nm and ∼680 nm with their energy difference equaling the spin-orbit coupling energy. The decrease in the PL signal intensity from location D to location F (*i.e.*, intensity decreases with increasing flake thickness) is in agreement with the Raman results providing extra proof for the correctness of the layer thicknesses reported earlier in this work. Thus, we conclude that the SHG and THG results reported in the main document have been obtained from single layer thick MoS_2 flakes (*i.e.*, from locations A and B). In addition, we note that the magnitudes of the SHG and THG power levels measured from the other single layer thick MoS_2 flake (*i.e.*, from locations D and E) are in agreement with the results presented in main document.

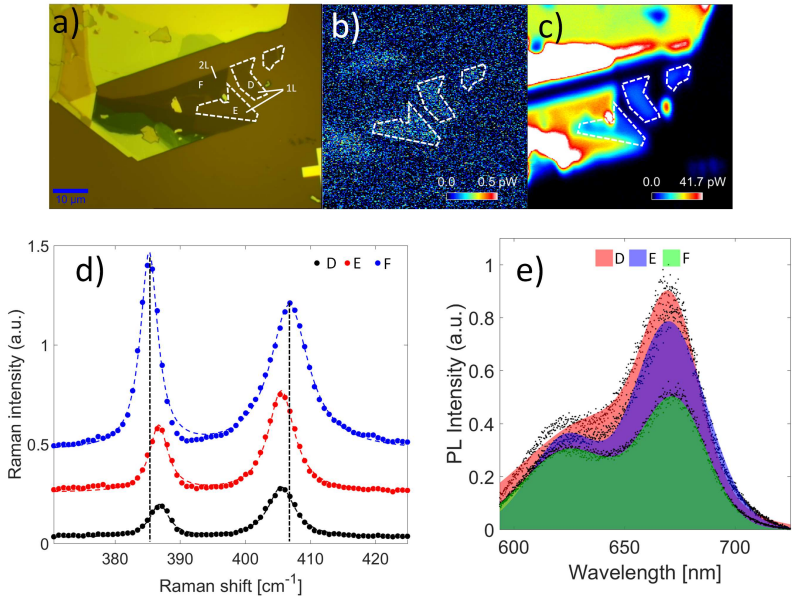

FIG. 3. Optical (a), SHG (b) and THG (c) images of the second MoS_2 flake. Raman (d) and PL (e) spectra from the areas marked with D-F in (a).

$MoSe_2$

Fig. 4 presents an optical image (discussed in the main document) of the $MoSe_2$ in addition to the Raman spectra measured from three different locations of the flake. Raman spectrum measured from the three areas of the flake (marked with letters G, H and I) is shown in Fig. 4(b). Three Raman modes are observed in Raman spectra close to the wavenumbers of ∼242 cm^{-1}, ∼285 cm^{-1} and ∼360 cm^{-1}. These Raman peaks originate from the out-of-plane A_{1g}, in-plane E^1_{2g} and B^1_{2g} vibration modes, respectively [19]. The location, shape and magnitude of these Raman modes can be used to extract the information related to $MoSe_2$ layer thickness. For example, for single layer and bilayer thick $MoSe_2$ flake the out-of-plane A_{1g} has been observed to locate at the wavenumbers of ∼240 cm^{-1} and ∼241 cm^{-1}, respectively, and shift to larger wavenumbers with increasing flake thickness. Thus, the location of the A_{1g} Raman mode for location G (240.4 cm^{-1}), for location H (241.2 cm^{-1}) and for location I (241.3 cm^{-1}) implies that $MoSe_2$ flake is thicker at locations H and I compared to location G. Furthermore, Tonndorf *et al.* observed that the A_{1g} Raman mode possesses sidepeaks due to Davydov splitting when the flake thickness is larger than two layers. No such sidepeaks are observed in our case which would then suggest that the $MoSe_2$ flake is thinner than three layers at all these locations (*i.e.*, single layer for location G and bilayer for location H and I). The following reasoning would also imply that SHG signal should not be observed at locations H and I because it would then possess even number of layers which is in contrast to what we see for location H in SHG image (see Fig. 2 in the main text). On the other hand, we observe no SHG signal at location I suggesting that $MoSe_2$ possesses odd number of layers at that location. Therefore, the more probable explanation is that we observe no such sidepeaks in our measurements and that the flake is the thinnest at location G (*i.e.*, single layer), location H possesses odd number of layers (*i.e.*, three layers) and location I is the thickest of these locations (*i.e.* at least four layers thick). More information from the flake thickness can be obtained by studying the B^1_{2g} vibration mode because the strength of this Raman mode is expected to decrease with increasing layer thickness. Furthermore, B^1_{2g} vibration mode was not resolved from single layer $MoSe_2$ and was the strongest in bilayer $MoSe_2$[19]. In our case B^1_{2g} Raman mode is not observed at location G but is clearly visible at the location H and location I. Therefore, the intensity level of B^1_{2g} vibration mode at different locations agrees with the previous discussion and we conclude that the $MoSe_2$ flake at location G is single layer thick.

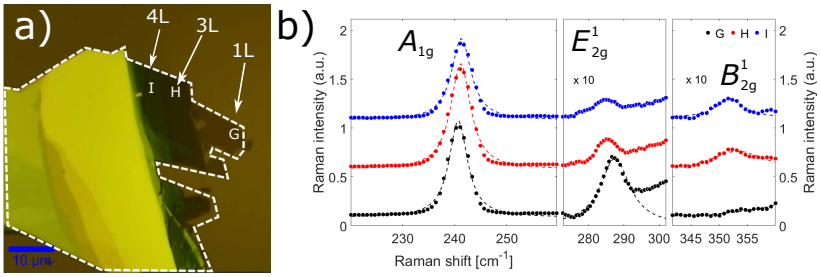

FIG. 4. (a) Optical image of the $MoSe_2$ flake. (b) Raman spectra measured from the areas marked with G-I in (a).

To further verify that no sidepeaks are observed in A_{1g} Raman peak and to gather more statistical credibility other $MoSe_2$ flakes were characterized as well. Fig. 5 presents the optical, SHG and THG images of another $MoSe_2$ flake in addition to the μ-Raman and μ-PL spectra measured from four different locations of the flake. Similarly as before three Raman modes are observed, see Fig. 5(d). The behavior of these Raman peaks is similar to that discussed earlier. However, this time no SHG signal is observed from location K and M. Thus, following the same reasoning as above $MoSe_2$ flake is single-layer, bilayer, three layers and four layers thick in locations J, K, L and M, respectively. To further confirm the observations, μ-PL was measured from the same areas (see Fig.5(e)). As shown, the intensity of the PL signal is the strongest at location J, and reduces with increasing layer thickness. This is expected behavior for atomically thin TMD layers when their thickness increases. In addition, the peak maximum at 787 nm and at 807 nm for single layer and bilayer $MoSe_2$ is in agreement with the literature[19]. As a result, we conclude that the SHG and THG results reported in the main document (obtained from location G) have been measured from single layer thick $MoSe_2$ flakes. Once again, the magnitudes of the SHG and THG power levels measured from other single layer thick $MoSe_2$ flakes (*e.g.*, from location J) are in agreement with the results presented in main document.

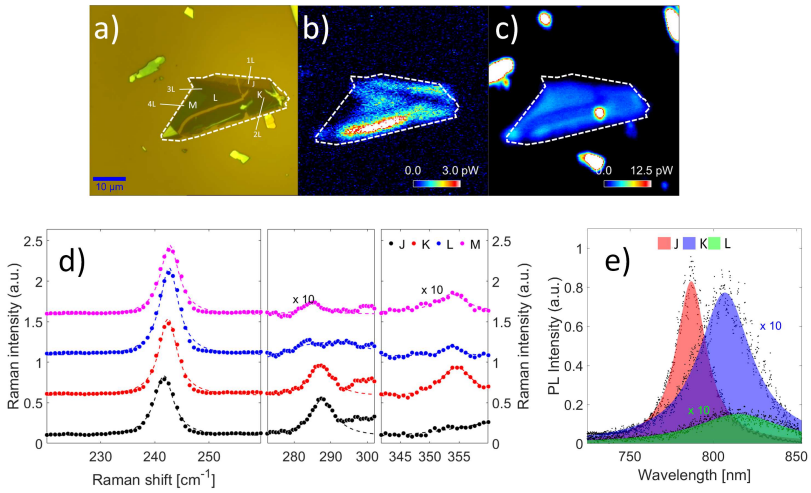

FIG. 5. Optical (a), SHG (b) and THG (c) images of the second $MoSe_2$ flake. Raman (d) and PL (e) spectra from the areas marked with J-M in (a).

WS_2

Fig. 6 presents an optical image of the WS_2 flake (location N) in addition to the measured Raman spectrum. This WS_2 flake locates in Fig. 1(a) close to the other transferred TMD materials. No SHG signal is observed from this flake (see Fig. 1(a)), which implies that the layer number is even (*i.e.* flake is at least bilayer thick). The Raman spectrum of the same flake is shown in Fig. 6(b). Two Raman modes are observed from the spectrum at wavenumbers of ∼355 cm^{-1} and ∼420 cm^{-1}. We attribute the Raman mode at ∼355 cm^{-1} to E^1_{2g} phonon overlapped by second-order LA(M) phonon (as seen from the fitting results) similarly as that reported earlier with resonant Raman scattering studies performed with 514 nm laser excitation [21]. The Raman mode at ∼420 cm^{-1} is due to A_{1g} vibration mode also agreeing with the literature. The Raman peak separation can be used to extract the layer thickness from the Raman data (*i.e.* peak separation increases with increasing flake thickness)[21]. In our case, Raman peak separation of 59.8 $^{-1}$ cm^{-1} can be obtained which is smaller than that reported in ref. 21 for bilayer WS_2 flakes (∼63 $^{-1}$ cm^{-1}) by using a 514 nm excitation in Raman measurements. Thus, all results suggest that the WS_2 crystal at location N is bilayer thick.

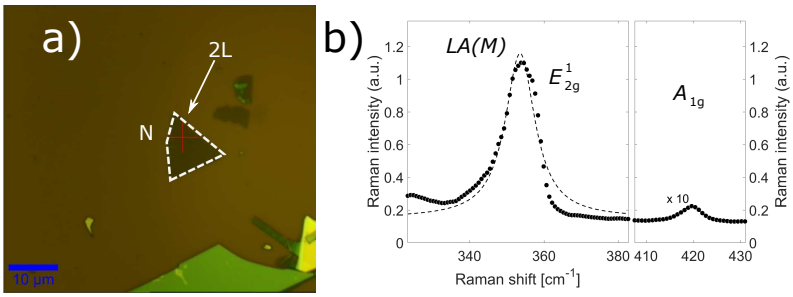

FIG. 6. Optical image (a) and Raman spectra (b) of the bilayer WS_2 flake.

As mentioned in the main document, the SHG and THG power levels used in this work were always taken from the measurements of a single layer thick flakes. Therefore, we also transferred another WS_2 flake close to the measurement area. Note that this flake was transferred a bit further away from the region presented in Fig. 1(a) in the main text (and also in Fig. 1.) and is therefore shown in the inset. Fig. 7 shows an optical image of that WS_2 flake in addition to the measured Raman spectrum. As observed, this WS_2 flake possesses one extremely thin area (labeled as area O) and one thicker area (labeled as area P). This time SHG signal is observed from location O implying that the layer number in that location is odd. In addition to this, SHG signal is also observed from the area (marked with letter Q) near this flake. On the other hand, no SHG signal is observed from the area P.

Raman and PL spectra was measured to obtain the layer thickness for the thin region. This time Raman spectrum

shows only contribution from the E^1_{2g} vibration mode overlapped by the LA(M) phonon at 356.1 cm^{-1} for location O. Therefore, the Raman peak separation couldn't be accurately estimated from Raman data for location O. We note that the Raman spectrum from area P shows the typical Raman modes of WS_2. Therefore, it seems that the intensity of A_{1g} Raman mode for thin WS_2 flakes can be below the noise level of our Raman system. However, the layer thickness at location O can be obtained from the PL spectrum (shown in Fig. 7(e)). Strong PL is observed at the wavelength of 614 nm which agrees well with the exciton A transition for single layer WS_2. We note that PL intensity reduces and also redshifts approaching to a value of ∼640nm for thicker WS_2 flakes. Therefore, we conclude that the area O is single layer thick WS_2. Also we note that the SHG and THG results reported in the main document have been obtained from the location O.

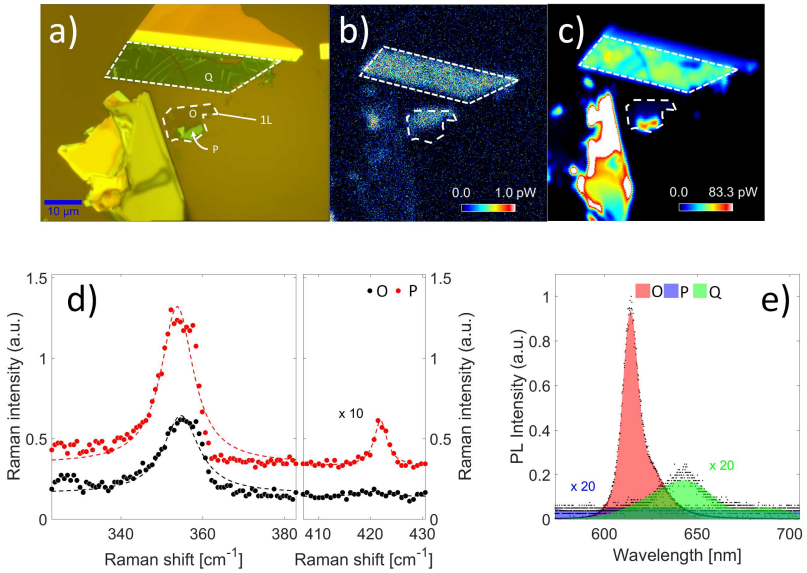

FIG. 7. Optical (a), SHG (b) and THG (c) images of the second WS_2 flake. Raman (d) and PL (e) spectra from the areas marked with O-Q in (a).

WSe_2

Fig. 8 presents an optical image of the WSe_2 flake (labeled as location R) in addition to the measured Raman spectrum. As presented, SHG signal is observed from this flake (see Fig. 2 in the main text) which implies that the flake is comprised of odd number of WSe_2 layers. To verify experimentally the flake thickness, Raman spectrum of the flake was measured (shown in Fig. 8(b)). Raman spectrum of WSe_2 flake shows Raman peak at wavenumber of 260 cm^{-1}. Typically, Raman spectrum of exfoliated WSe_2 possesses fingerprint from two Raman modes, one near the wavenumber of ∼260 cm^{-1} (as seen in our spectrum) and another near the wavenumber of ∼309 cm^{-1} (not seen in our spectrum). Previously, these peaks have been addressed to the in-plane E^1_{2g} vibration mode (possibly with a fingerprint from the out-of-plane A_{1g} vibration mode) and B_{2g} vibration modes, respectively[19]. It has been observed that the Raman peak at ∼260 cm^{-1} is strong (as we also observe in our case) for single to few layer thick WSe_2. On the other hand, the Raman peak near the wavenumber of ∼309 cm^{-1} should only be visible for WSe_2 flakes thicker than bilayer WSe_2. Therefore, as we see no traces from that Raman mode in our spectrum we conclude that WSe_2 at the location R is single layer thick.

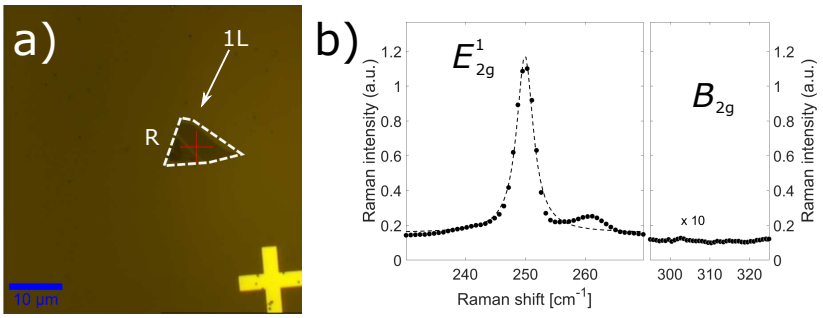

FIG. 8. Optical image (a) and Raman spectra (b) of the WSe_2 flake discussed in the main text.

We also show optical, SHG and THG images of another WSe_2 flake in addition to the measured Raman and PL spectrum from four different locations (labeled with letters S, T, U and V); see Fig. 9. As shown, SHG signal is observed from locations S, T and U implying that flake is comprised of odd number of layers whereas for location V no SHG signal is observed suggesting even number layer thickness. The Raman spectrum measured from each location are presented in Fig. 9(d). The Raman spectrum of location S is similar than that of location R thereby suggesting that the WSe_2 flake thickness at the location S is identical to location R (*i.e.*, single layer). For location T, V and U, B_{2g} vibration mode is observed implying that the WSe_2 flake thickness is either 3 or 5 layers (at location T) and larger than ¿10 layers at the two latter areas. Furthermore, Fig. 9(e) plots the μ-PL spectrum of locations S, T and U. Strong PL with peak wavelength at 747.5 nm is observed at location S in agreement with literature reports of PL studies performed to single layer thick WSe_2 flakes. The PL redshifts and weakens at locations T and U also agreeing with the literature reports of few-layer thick WSe_2 flakes. Thus, we conclude that SHG and THG values reported in main document (obtained from location R) are taken from single layer thick WSe_2 material. Also we note that SHG and THG power levels measured from location S are in agreement with the values measured from location R providing more statistical credibility to the reported values.

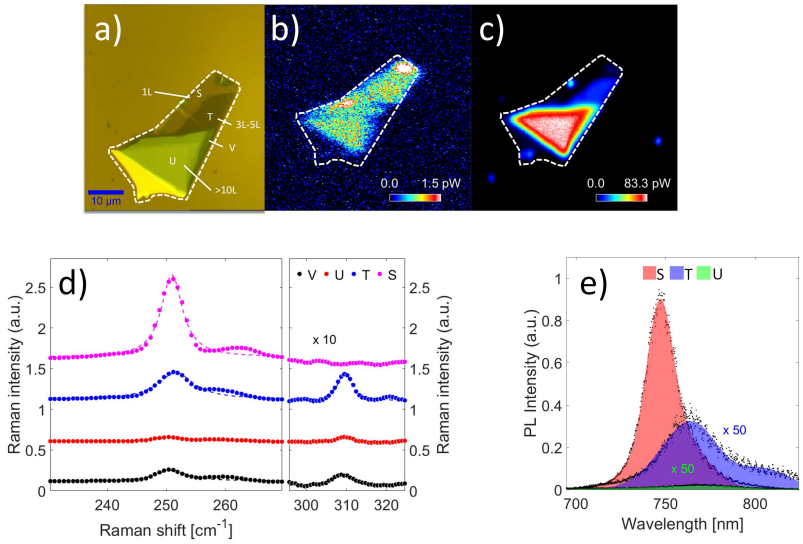

FIG. 9. Optical (a), SHG (b) and THG (c) images of the second WSe_2 flake. Raman (d) and PL (e) spectra from the areas marked with S-V in (a).

POWER SERIES MEASUREMENTS

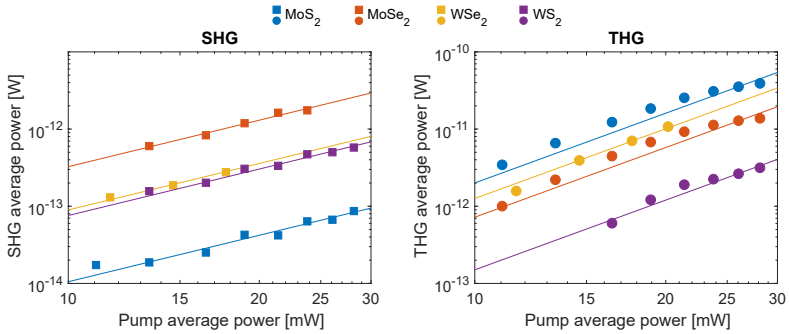

FIG. 10. Power series measurements of all four TMDs.

THEORETICAL CALCULATION OF NONLINEAR COEFFICIENTS

Here we calculate the nonlinear susceptibilities of MoS_2, $MoSe_2$, WS_2, and WSe_2 starting from a tight-binding (TB) description of the electronic band structure of these materials[22] and studying the dynamics by means of Bloch equations for the valence and conduction bands, with an additional excitonic band included in the case of $MoSe_2$. The relevant valence and conduction band regions (closer to the band gap) is around the K band edges, where one can approximate the system as a two-band $\mathbf{k}\cdot\mathbf{p}$ Hamiltonian $\mathcal{H}_0(\mathbf{k},\tau,s) = \mathcal{H}_1(\mathbf{k},\tau,s) + \mathcal{H}_2(\mathbf{k},\tau) + \mathcal{H}_3(\mathbf{k},\tau)$. The terms in this Hamiltonian are

$$\mathcal{H}_1(\mathbf{k},\tau,s) = \begin{bmatrix} \frac{\Delta}{2} & t_0 a(\tau k_x - i k_y) \\ t_0 a(\tau k_x + i k_y) & \tau s\Lambda - \frac{\Delta}{2} \end{bmatrix}, \tag{1}$$

$$\mathcal{H}_2(\mathbf{k},\tau,s) = \begin{bmatrix} \gamma_1 a^2 k^2 & \gamma_3 a^2(\tau k_x + i k_y)^2 \\ \gamma_3 a^2(\tau k_x - i k_y)^2 & \gamma_2 a^2 k^2 \end{bmatrix}, \tag{2}$$

$$\mathcal{H}_3(\mathbf{k},\tau,s) = \begin{bmatrix} \gamma_4 a^3 \tau k_x(k_x^2 - 3k_y^2) & \gamma_6 a^3 k^2(\tau k_x - i k_y) \\ \gamma_6 a^3 k^2(\tau k_x + i k_y) & \gamma_5 a^3 \tau k_x(k_x^2 - 3k_y^2) \end{bmatrix}, \tag{3}$$

where $\tau, s = \pm 1$ label non-degenerate valleys and spins and $\mathbf{k} = (k_x\ k_y)$ is the electron wave vector. The parameters of $\mathcal{H}_0(\mathbf{k},\tau,s)$, obtained by fitting the TB valence and conduction energy bands with the ones obtained from first-principles GW simulations[22], are listed in Table S1. It should be noted that such a Hamiltonian accounts for both non-degenerate valleys and spin-orbit coupling.

We calculate the optical constants through a perturbative expansion of $\mathcal{H}_0(\boldsymbol{\kappa}(t),\tau,s)$, using the minimum coupling prescription for the electron quasi-momentum: $\hbar\boldsymbol{\kappa}(t) = \hbar\mathbf{k} + e\mathbf{A}(t)$, where e is the electron charge and $\mathbf{A}(t)$ is the

TABLE S2. Fitted constants of the the two-band $\mathbf{k}\cdot\mathbf{p}$ Hamiltonian $\mathcal{H}_0(\mathbf{k},\tau,s)$.

Constants	MoS_2	$MoSe_2$	WS_2	WSe_2
a (Å)	3.190	3.326	3.191	3.325
Δ (eV)	1.658	1.429	1.806	1.541
t_0 (eV)	0.933	0.768	1.196	1.016
Λ (eV)	0.073	0.091	0.211	0.228
γ_1 (eV)	0.351	0.291	0.443	0.404
γ_2 (eV)	−0.198	−0.191	−0.211	−0.216
γ_3 (eV)	−0.143	−0.099	−0.199	−0.150
γ_4 (eV)	0.058	0.038	0.171	0.117
γ_5 (eV)	0.038	0.055	−0.030	0.003
γ_6 (eV)	−0.368	−0.356	−0.450	−0.453

potential vector of the impinging light. With this prescription, we define unperturbed and interacting Hamiltonians $\mathcal{H}_0(\mathbf{k},\tau,s)$ and $\mathcal{H}_\mathrm{I}(\mathbf{k},\tau,s,t)$, respectively, and write the total Hamiltonian as $\mathcal{H}_\mathrm{T}(\mathbf{k},\tau,s,t) = \mathcal{H}_0[\boldsymbol{\kappa}(t),\tau,s] = \mathcal{H}_0(\mathbf{k},\tau,s) + \mathcal{H}_\mathrm{I}(\mathbf{k},\tau,s,t)$, where

$$\begin{aligned}\mathcal{H}_\mathrm{I}(\mathbf{k},\tau,s,t) = \frac{e}{\hbar}[D_x A_x(t) + D_y A_y(t)] + \frac{e^2}{\hbar^2}[D_{xx}A_x^2(t) + D_{xy}A_x(t)A_y(t) + D_{yy}A_y^2(t)] + \\ + \frac{e^3}{\hbar^3}[D_{xxx}A_x^3(t) + D_{xxy}A_x^2(t)A_y(t) + D_{xyy}A_x(t)A_y^2(t) + D_{yyy}A_y^3(t)],\end{aligned} \tag{4}$$

and the interaction operators in the expression above are explicitly given by

$$\begin{aligned}
D_x &= t_0 a\tau\left[|\psi_\mathrm{V}\rangle\langle\psi_\mathrm{C}| + |\psi_\mathrm{C}\rangle\langle\psi_\mathrm{V}|\right],\\
D_y &= it_0 a\left[|\psi_\mathrm{V}\rangle\langle\psi_\mathrm{C}| - |\psi_\mathrm{C}\rangle\langle\psi_\mathrm{V}|\right],\\
D_{xx} &= \gamma_1 a^2|\psi_\mathrm{C}\rangle\langle\psi_\mathrm{C}| + \gamma_2 a^2|\psi_\mathrm{V}\rangle\langle\psi_\mathrm{V}| + \gamma_3 a^2\left[|\psi_\mathrm{V}\rangle\langle\psi_\mathrm{C}| + |\psi_\mathrm{C}\rangle\langle\psi_\mathrm{V}|\right],\\
D_{yy} &= \gamma_1 a^2|\psi_\mathrm{C}\rangle\langle\psi_\mathrm{C}| + \gamma_2 a^2|\psi_\mathrm{V}\rangle\langle\psi_\mathrm{V}| - \gamma_3 a^2\left[|\psi_\mathrm{V}\rangle\langle\psi_\mathrm{C}| + |\psi_\mathrm{C}\rangle\langle\psi_\mathrm{V}|\right],\\
D_{xy} &= 2i\gamma_3 a^2\tau\left[|\psi_\mathrm{C}\rangle\langle\psi_\mathrm{V}| - |\psi_\mathrm{V}\rangle\langle\psi_\mathrm{C}|\right],\\
D_{xxx} &= \gamma_4 a^3\tau|\psi_\mathrm{C}\rangle\langle\psi_\mathrm{C}| + \gamma_5 a^3\tau|\psi_\mathrm{V}\rangle\langle\psi_\mathrm{V}| + \gamma_6 a^3\tau\left[|\psi_\mathrm{V}\rangle\langle\psi_\mathrm{C}| + |\psi_\mathrm{C}\rangle\langle\psi_\mathrm{V}|\right],\\
D_{xxy} &= i\gamma_6 a^3\left[|\psi_\mathrm{V}\rangle\langle\psi_\mathrm{C}| - |\psi_\mathrm{C}\rangle\langle\psi_\mathrm{V}|\right],\\
D_{xyy} &= -3\gamma_4 a^3\tau|\psi_\mathrm{C}\rangle\langle\psi_\mathrm{C}| - 3\gamma_5 a^3\tau|\psi_\mathrm{V}\rangle\langle\psi_\mathrm{V}| + \gamma_6 a^3\tau\left[|\psi_\mathrm{V}\rangle\langle\psi_\mathrm{C}| + |\psi_\mathrm{C}\rangle\langle\psi_\mathrm{V}|\right],\\
D_{yyy} &= i\gamma_6 a^3\left[|\psi_\mathrm{V}\rangle\langle\psi_\mathrm{C}| - |\psi_\mathrm{C}\rangle\langle\psi_\mathrm{V}|\right].
\end{aligned}$$

Here, we have used the Dirac notation for the conduction $|\psi_\mathrm{C}\rangle$ and valence $|\psi_\mathrm{V}\rangle$ band eigenstates, and we have approximated the matrix elements by their values at the band edges ($\mathbf{k} = 0$). Inserting the Ansatz $|\psi\rangle = c_-|\psi_\mathrm{V}\rangle + c_+|\psi_\mathrm{C}\rangle$ in the time-dependent Schrödinger equation $i\hbar\partial_t|\psi\rangle = \mathcal{H}_\mathrm{T}|\psi\rangle$, and defining the inversion population $n_\mathbf{k} = |c_+|^2 - |c_-|^2$ and the interband coherence $\rho_\mathbf{k} = c_+c_-^*$, one gets

$$\begin{aligned}
\dot\rho_\mathbf{k} = &-\frac{i}{\hbar}(E_\mathrm{C} - E_\mathrm{V})\rho_\mathbf{k} - \gamma\rho_\mathbf{k} + \frac{ie}{\hbar^2}n_\mathbf{k}\Big\{D_x^\mathrm{CV}A_x(t) + D_y^\mathrm{CV}A_y(t) + \frac{e}{\hbar}[D_{xx}^\mathrm{CV}A_x^2(t) + D_{xy}^\mathrm{CV}A_x(t)A_y(t) + \\
&+D_{yy}^\mathrm{CV}A_y^2(t)] + \frac{e^2}{\hbar^2}[D_{xxx}^\mathrm{CV}A_x^3(t) + D_{xxy}^\mathrm{CV}A_x^2(t)A_y(t) + D_{xyy}^\mathrm{CV}A_x(t)A_y^2(t) + D_{yyy}^\mathrm{CV}A_y^3(t)]\Big\} + \\
&+\frac{ie^2}{\hbar^3}\left\{(D_{xx}^\mathrm{VV} - D_{xx}^\mathrm{CC})A_x^2(t) + (D_{yy}^\mathrm{VV} - D_{yy}^\mathrm{CC})A_y^2(t) + \right. \\
&\left.+\frac{e}{\hbar}[(D_{xxx}^\mathrm{VV} - D_{xxx}^\mathrm{CC})A_x^3(t) + (D_{xyy}^\mathrm{VV} - D_{xyy}^\mathrm{CC})A_x(t)A_y^2(t)]\right\}\rho_\mathbf{k},
\end{aligned} \tag{5}$$

$$\begin{aligned}
\dot n_\mathbf{k} = &-\frac{4e}{\hbar^2}\mathrm{Im}\Big\{\rho_\mathbf{k}\Big[D_x^\mathrm{VC}A_x(t) + D_y^\mathrm{VC}A_y(t) + \frac{e}{\hbar}[D_{xx}^\mathrm{VC}A_x^2(t) + D_{xy}^\mathrm{VC}A_x(t)A_y(t) + D_{yy}^\mathrm{VC}A_y^2(t)] + \\
&+\frac{e^2}{\hbar^2}[D_{xxx}^\mathrm{VC}A_x^3(t) + D_{xxy}^\mathrm{VC}A_x^2(t)A_y(t) + D_{xyy}^\mathrm{VC}A_x(t)A_y^2(t) + D_{yyy}^\mathrm{VC}A_y^3(t)]\Big]\Big\},
\end{aligned} \tag{6}$$

where $E_\mathrm{C}(\mathbf{k})$ and $E_\mathrm{V}(\mathbf{k})$ are the conduction and valence energy bands of the unperturbed Hamiltonian $\mathcal{H}_0$, $D_j^\mathrm{CV} = \langle\psi_\mathrm{C}|D_j|\psi_\mathrm{V}\rangle$ are the interaction matrix elements, and we have introduced a phenomenological relaxation rate $\gamma = 10$ ps^{-1} accounting for dephasing.

In order to obtain the nonlinear susceptibilities, we consider a monochromatic optical field $\mathbf{E}(t) = \mathrm{Re}\left\{\mathbf{E}_0\mathrm{e}^{-i\omega t}\right\}$ with angular frequency ω for which $\mathbf{A}(t) = \mathrm{Re}\left\{(\mathbf{E}_0/i\omega)\mathrm{e}^{-i\omega t}\right\}$. We then solve perturbatively the equations above in the weak excitation limit $n_\mathbf{k} \approx -1$ by taking the Ansatz $\rho_\mathbf{k} = \sum_{j=-3}^{+3}\rho_j^{(j/|j|)}\mathrm{e}^{ji\omega t}$ and obtaining analytical expressions for the coefficients $\rho_j^{(j/|j|)}$. We find the macroscopic surface current density to be given by

$$\mathbf{J}(t) = -\frac{e}{4\pi^2\hbar}\sum_{\tau,s=-1,1}\int_{-\infty}^{+\infty}dk_x\int_{-\infty}^{+\infty}dk_y\left[\langle\psi(t)|\nabla_\mathbf{k}\mathcal{H}_\mathrm{T}(t)|\psi(t)\rangle - \langle\psi_\mathrm{V}|\nabla_\mathbf{k}\mathcal{H}_\mathrm{T}(t)|\psi_\mathrm{V}\rangle\right], \tag{7}$$

while the polarization, obtained as $\mathbf{P}(t) = (1/d)\int_{-\infty}^{t}dt'\mathbf{J}(t')$, where d is the material thickness, can be expressed as

$$\mathbf{P}(t) = \epsilon_0\mathrm{Re}\left[\hat\chi^{(1|\omega)}\mathbf{E}_0\mathrm{e}^{-i\omega t} + \hat\chi^{(3|\omega)}\mathbf{E}_0^*\mathbf{E}_0\mathbf{E}_0\mathrm{e}^{-i\omega t} + \hat\chi^{(2|2\omega)}\mathbf{E}_0\mathbf{E}_0\mathrm{e}^{-2i\omega t} + \hat\chi^{(3|3\omega)}\mathbf{E}_0\mathbf{E}_0\mathbf{E}_0\mathrm{e}^{-3i\omega t}\right].$$

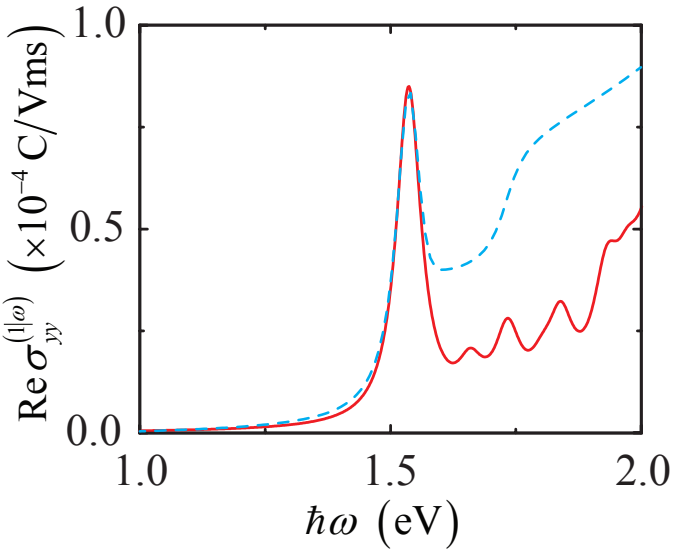

FIG. 11. Comparison of the real part of the linear conductivity $\mathrm{Re}\sigma_{yy}^{(1|\omega)}$ obtained through the Bethe-Salpeter approach (red full curve) and the three-band effective model (blue dashed curve). While we find excellent matching in the low-energy limit, the three-band model is insufficient to capture high-energy resonances observed in Bethe-Salpeter calculations.

Here, $\hat{\chi}^{(l|m\omega)}$ $(l, m = 1, 2, 3)$ are the linear and nonlinear susceptibility tensors and ϵ_0 is the vacuum permittivity. Because in the notation used centrosymmetry is broken along the y-direction, the relevant components of the susceptibility tensors for comparison with measurements are the ones corresponding to an optical field polarized along the y-direction, for which

$$\chi_{yy}^{(1|\omega)} = \frac{e^2}{4\pi^2\epsilon_0\hbar^2\omega^2 d}\sum_{\tau,s=\pm1}\int_{-\infty}^{+\infty}dk_x\int_{-\infty}^{+\infty}dk_y\left\{\frac{|D_y^{\mathrm{CV}}|^2}{[(E_{\mathrm{C}}-E_{\mathrm{V}})-\hbar(\omega+i\gamma)]}+\right. \tag{8}$$
$$\left.+\frac{|D_y^{\mathrm{CV}}|^2}{[(E_{\mathrm{C}}-E_{\mathrm{V}})+\hbar(\omega+i\gamma)]}\right\},$$

$$\chi_{yyy}^{(2|2\omega)} = -\frac{ie^3}{16\pi^2\epsilon_0\hbar^3\omega^3 d}\sum_{\tau,s=\pm1}\int_{-\infty}^{+\infty}dk_x\int_{-\infty}^{+\infty}dk_y\left\{\frac{2D_y^{\mathrm{CV}}D_{yy}^{\mathrm{VC}}}{[(E_{\mathrm{C}}-E_{\mathrm{V}})-\hbar(\omega+i\gamma)]}+\right. \tag{9}$$
$$\left.+\frac{2D_y^{\mathrm{VC}}D_{yy}^{\mathrm{CV}}}{[(E_{\mathrm{C}}-E_{\mathrm{V}})+\hbar(\omega+i\gamma)]}+\frac{D_y^{\mathrm{VC}}D_{yy}^{\mathrm{CV}}}{[(E_{\mathrm{C}}-E_{\mathrm{V}})-\hbar(2\omega+i\gamma)]}+\frac{D_y^{\mathrm{CV}}D_{yy}^{\mathrm{VC}}}{[(E_{\mathrm{C}}-E_{\mathrm{V}})+\hbar(2\omega+i\gamma)]}\right\},$$

$$\chi_{yyyy}^{(3|3\omega)} = -\frac{e^4}{48\pi^2\epsilon_0\hbar^4\omega^4 d}\sum_{\tau,s=\pm1}\int_{-\infty}^{+\infty}dk_x\int_{-\infty}^{+\infty}dk_y\left\{\frac{D_y^{\mathrm{VC}}D_{yyy}^{\mathrm{CV}}}{[(E_{\mathrm{C}}-E_{\mathrm{V}})-\hbar(3\omega+i\gamma)]}+\right. \tag{10}$$
$$+\frac{D_y^{\mathrm{CV}}D_{yyy}^{\mathrm{VC}}}{[(E_{\mathrm{C}}-E_{\mathrm{V}})+\hbar(3\omega+i\gamma)]}+\frac{2|D_{yy}^{\mathrm{VC}}|^2}{[(E_{\mathrm{C}}-E_{\mathrm{V}})-\hbar(2\omega+i\gamma)]}+\frac{2|D_{yy}^{\mathrm{VC}}|^2}{[(E_{\mathrm{C}}-E_{\mathrm{V}})+\hbar(2\omega+i\gamma)]}+$$
$$\left.+\frac{3D_y^{\mathrm{CV}}D_{yyy}^{\mathrm{VC}}}{[(E_{\mathrm{C}}-E_{\mathrm{V}})-\hbar(\omega+i\gamma)]}+\frac{3D_y^{\mathrm{VC}}D_{yyy}^{\mathrm{CV}}}{[(E_{\mathrm{C}}-E_{\mathrm{V}})+\hbar(\omega+i\gamma)]}\right\}.$$

Data reported in the main paper for MoS_2, WS_2, and WSe_2 are obtained through the expressions above. Unlike the other ML TMDs, at a photon energy of $\hbar\omega = 0.8$ eV, $MoSe_2$ undergoes second-harmonic generation matching the exciton resonance at 1.6 eV, and thus, this material requires a more involved theoretical treatment accounting for excitons. We describe the exciton resonance as an effective energy level $E_{\mathrm{ex}}(\mathbf{k})$ (and its corresponding eigenstate $|\psi_{\mathrm{ex}}\rangle$) lying within the bandgap of the unperturbed single-particle Hamiltonian, which for this material becomes

$$\mathcal{H}_0(\mathbf{k},\tau,s) = E_{\mathrm{ex}}(\mathbf{k})|\psi_{\mathrm{ex}}\rangle\langle\psi_{\mathrm{ex}}| + E_{\mathrm{V}}(\mathbf{k},\tau,s)|\psi_{\mathrm{V}}\rangle\langle\psi_{\mathrm{V}}| + E_{\mathrm{C}}(\mathbf{k},\tau,s)|\psi_{\mathrm{C}}\rangle\langle\psi_{\mathrm{C}}|, \tag{11}$$

while the interaction Hamiltonian becomes

$$\begin{aligned}\mathcal{H}_{\rm I}(\mathbf{k},\tau,s,t) = &\frac{e}{\hbar}[D_x A_x(t) + D_y A_y(t)] + \frac{e^2}{\hbar^2}[D_{xx}A_x^2(t) + D_{xy}A_x(t)A_y(t) + D_{yy}A_y^2(t)] + \\ &+ \frac{e^3}{\hbar^3}[D_{xxx}A_x^3(t) + D_{xxy}A_x^2(t)A_y(t) + D_{xyy}A_x(t)A_y^2(t) + D_{yyy}A_y^3(t)] + \\ &+ \frac{e}{\hbar}C_{\rm ex}\left[|\psi_{\rm V}\rangle\langle\psi_{\rm ex}| + |\psi_{\rm ex}\rangle\langle\psi_{\rm V}| + |\psi_{\rm C}\rangle\langle\psi_{\rm ex}| + |\psi_{\rm ex}\rangle\langle\psi_{\rm C}|\right][A_x(t) + A_y(t)],\end{aligned} \tag{12}$$

where $C_{\rm ex}$ is the transition matrix element coupling the effective exciton band with the valence and conduction bands. This allows us to obtain the linear conductivity following the same approach described above

$$\begin{aligned}\sigma_{yy}^{(1|\omega)} = &\frac{-ie^2}{4\pi^2\hbar^2\omega}\sum_{\tau,s=\pm1}\int_{-\infty}^{+\infty}dk_x\int_{-\infty}^{+\infty}dk_y\left\{\frac{|D_y^{\rm CV}|^2}{[(E_{\rm C}-E_{\rm V})-\hbar(\omega+i\gamma)]}+\right. \\ &\left.+\frac{|D_y^{\rm CV}|^2}{[(E_{\rm C}-E_{\rm V})+\hbar(\omega+i\gamma)]}+\frac{C_{\rm ex}^2}{[(E_{\rm ex}-E_{\rm V})-\hbar(\omega+i\gamma)]}+\frac{C_{\rm ex}^2}{[(E_{\rm ex}-E_{\rm V})+\hbar(\omega+i\gamma)]}\right\},\end{aligned} \tag{13}$$

using the transition matrix element $C_{\rm ex}$ as a free parameter. We adjust this parameter in order to obtain best agreement with respect to first-principles simulations of the linear conductivity based upon the Bethe-Salpeter approach[23] [see Fig. S9 where we compare the linear conductivities obtained through the effective three band model and the Bethe-Salpeter approach]. Once the transition matrix element is fixed to $C_{\rm ex} = 1.019$ meV·nm, and the exciton energy band to $E_{\rm ex} = E_{\rm V} + \mathcal{E}$ with $\mathcal{E} = 1.536$ eV, we calculate the nonlinear conductivities following the same approach we have illustrated above obtaining

$$\begin{aligned}\chi_{yyy}^{(2|2\omega)} = &-\frac{ie^3}{16\pi^2\epsilon_0\hbar^3\omega^3 d}\sum_{\tau,s=\pm1}\int_{-\infty}^{+\infty}dk_x\int_{-\infty}^{+\infty}dk_y\left\{\frac{2D_y^{\rm CV}D_{yy}^{\rm VC}}{[(E_{\rm C}-E_{\rm V})-\hbar(\omega+i\gamma)]}+\right. \\ &+\frac{2D_y^{\rm VC}D_{yy}^{\rm CV}}{[(E_{\rm C}-E_{\rm V})+\hbar(\omega+i\gamma)]}+\frac{D_y^{\rm VC}D_{yy}^{\rm CV}}{[(E_{\rm C}-E_{\rm V})-\hbar(2\omega+i\gamma)]}+\frac{D_y^{\rm CV}D_{yy}^{\rm VC}}{[(E_{\rm C}-E_{\rm V})+\hbar(2\omega+i\gamma)]}+ \\ &+\frac{D_y^{\rm VC}C_{\rm ex}^2(2E_{\rm ex}-E_{\rm V}-E_{\rm C}+2i\hbar\gamma)}{[(E_{\rm C}-E_{\rm ex})+\hbar(2\omega-i\gamma)]\,[(E_{\rm C}-E_{\rm V})+\hbar(\omega+i\gamma)]\,[(E_{\rm ex}-E_{\rm V})+\hbar(2\omega+i\gamma)]}+ \\ &-\frac{D_y^{\rm VC}C_{\rm ex}^2(2E_{\rm C}-E_{\rm V}-E_{\rm ex}-2i\hbar\gamma)}{[(E_{\rm C}-E_{\rm ex})+\hbar(2\omega-i\gamma)]\,[(E_{\rm C}-E_{\rm V})-\hbar(2\omega+i\gamma)]\,[(E_{\rm ex}-E_{\rm V})-\hbar(\omega+i\gamma)]}+ \\ &+\frac{D_y^{\rm CV}C_{\rm ex}^2(2E_{\rm ex}-E_{\rm V}-E_{\rm C}-2i\hbar\gamma)}{[(E_{\rm C}-E_{\rm ex})-\hbar(2\omega-i\gamma)]\,[(E_{\rm C}-E_{\rm V})-\hbar(\omega+i\gamma)]\,[(E_{\rm ex}-E_{\rm V})-\hbar(2\omega+i\gamma)]}+ \\ &\left.-\frac{D_y^{\rm CV}C_{\rm ex}^2(2E_{\rm C}-E_{\rm V}-E_{\rm ex}+2i\hbar\gamma)}{[(E_{\rm C}-E_{\rm ex})-\hbar(2\omega-i\gamma)]\,[(E_{\rm C}-E_{\rm V})+\hbar(2\omega+i\gamma)]\,[(E_{\rm ex}-E_{\rm V})+\hbar(\omega+i\gamma)]}\right\},\end{aligned} \tag{14}$$

$$\begin{aligned}\chi_{yyyy}^{(3|3\omega)} = &-\frac{e^4}{48\pi^2\epsilon_0\hbar^4\omega^4 d}\sum_{\tau,s=\pm1}\int_{-\infty}^{+\infty}dk_x\int_{-\infty}^{+\infty}dk_y\left\{\frac{D_y^{\rm CV}D_{yyy}^{\rm VC}}{[(E_{\rm C}-E_{\rm V})-\hbar(3\omega+i\gamma)]}+\right. \\ &+\frac{D_y^{\rm CV}D_{yyy}^{\rm VC}}{[(E_{\rm C}-E_{\rm V})+\hbar(3\omega+i\gamma)]}+\frac{2|D_{yy}^{\rm VC}|^2}{[(E_{\rm C}-E_{\rm V})-\hbar(2\omega+i\gamma)]}+\frac{2|D_{yy}^{\rm VC}|^2}{[(E_{\rm C}-E_{\rm V})+\hbar(2\omega+i\gamma)]}+ \\ &\left.+\frac{3D_y^{\rm CV}D_{yyy}^{\rm VC}}{[(E_{\rm C}-E_{\rm V})-\hbar(\omega+i\gamma)]}+\frac{3D_y^{\rm VC}D_{yyy}^{\rm CV}}{[(E_{\rm C}-E_{\rm V})+\hbar(\omega+i\gamma)]}+C_{\rm ex}^2 f(\mathbf{k},\omega)+C_{\rm ex}^4 g(\mathbf{k},\omega)\right\},\end{aligned} \tag{15}$$

where

$$\begin{aligned}g(\mathbf{k},\omega) = &\left\{[(E_{\rm ex}-E_{\rm V})+\hbar\tilde{\omega}_3]\,[(E_{\rm ex}-E_{\rm V})+\hbar\tilde{\omega}_1]\,[(E_{\rm C}-E_{\rm V})+\hbar\tilde{\omega}_2]\right\}^{-1}+ \\ &+\left\{[(E_{\rm ex}-E_{\rm V})-\hbar\tilde{\omega}_3]\,[(E_{\rm ex}-E_{\rm V})-\hbar\tilde{\omega}_1]\,[(E_{\rm C}-E_{\rm V})-\hbar\tilde{\omega}_2]\right\}^{-1}+ \\ &-\left\{[(E_{\rm ex}-E_{\rm V})+\hbar\tilde{\omega}_1]\,[(E_{\rm C}-E_{\rm ex})+\hbar\tilde{\omega}_3^*]\,[(E_{\rm C}-E_{\rm V})+\hbar\tilde{\omega}_2]\right\}^{-1}+ \\ &-\left\{[(E_{\rm ex}-E_{\rm V})-\hbar\tilde{\omega}_1]\,[(E_{\rm C}-E_{\rm ex})-\hbar\tilde{\omega}_3^*]\,[(E_{\rm C}-E_{\rm V})-\hbar\tilde{\omega}_2]\right\}^{-1},\end{aligned} \tag{16}$$

and

$$
\begin{aligned}
f(\mathbf{k},\omega) = & \frac{|D_y^{\mathrm{VC}}|^2}{[(E_{\mathrm{C}}-E_{\mathrm{V}})-\hbar\tilde{\omega}_3]\,[(E_{\mathrm{C}}-E_{\mathrm{V}})-\hbar\tilde{\omega}_1]\,[(E_{\mathrm{ex}}-E_{\mathrm{V}})-\hbar\tilde{\omega}_2]} + \\
& + \frac{|D_y^{\mathrm{VC}}|^2}{[(E_{\mathrm{C}}-E_{\mathrm{V}})+\hbar\tilde{\omega}_3]\,[(E_{\mathrm{C}}-E_{\mathrm{V}})+\hbar\tilde{\omega}_1]\,[(E_{\mathrm{ex}}-E_{\mathrm{V}})+\hbar\tilde{\omega}_2]} + \\
& - \frac{|D_y^{\mathrm{VC}}|^2\,[(E_{\mathrm{C}}-E_{\mathrm{ex}})-2\hbar\tilde{\omega}_1]}{[(E_{\mathrm{C}}-E_{\mathrm{V}})-\hbar\tilde{\omega}_3]\,[(E_{\mathrm{C}}-E_{\mathrm{ex}})-\hbar\tilde{\omega}_2^*]\,[(E_{\mathrm{ex}}-E_{\mathrm{V}})+\hbar\tilde{\omega}_1]\,[(E_{\mathrm{C}}-E_{\mathrm{V}})-\hbar\tilde{\omega}_1]} + \\
& + \frac{|D_y^{\mathrm{VC}}|^2\,[(E_{\mathrm{ex}}-E_{\mathrm{C}})-2\hbar\tilde{\omega}_1]}{[(E_{\mathrm{C}}-E_{\mathrm{V}})+\hbar\tilde{\omega}_3]\,[(E_{\mathrm{C}}-E_{\mathrm{ex}})+\hbar\tilde{\omega}_2^*]\,[(E_{\mathrm{ex}}-E_{\mathrm{V}})-\hbar\tilde{\omega}_1]\,[(E_{\mathrm{C}}-E_{\mathrm{V}})+\hbar\tilde{\omega}_1]} + \\
& - \frac{D_{yy}^{\mathrm{CV}}}{[(E_{\mathrm{ex}}-E_{\mathrm{V}})-\hbar\tilde{\omega}_3]\,[(E_{\mathrm{C}}-E_{\mathrm{V}})-\hbar\tilde{\omega}_2]} + \frac{D_{yy}^{\mathrm{VC}}}{[(E_{\mathrm{ex}}-E_{\mathrm{V}})+\hbar\tilde{\omega}_3]\,[(E_{\mathrm{C}}-E_{\mathrm{V}})+\hbar\tilde{\omega}_2]} + \\
& + \frac{2D_{yy}^{\mathrm{CV}}}{[(E_{\mathrm{ex}}-E_{\mathrm{V}})+\hbar\tilde{\omega}_1]\,[(E_{\mathrm{C}}-E_{\mathrm{V}})+\hbar\tilde{\omega}_2]} - \frac{2D_{yy}^{\mathrm{VC}}}{[(E_{\mathrm{ex}}-E_{\mathrm{V}})-\hbar\tilde{\omega}_1]\,[(E_{\mathrm{C}}-E_{\mathrm{V}})-\hbar\tilde{\omega}_2]} + \\
& + \frac{|D_y^{\mathrm{VC}}|^2\,[(E_{\mathrm{ex}}-E_{\mathrm{C}})-2\hbar\tilde{\omega}_1]}{[(E_{\mathrm{C}}-E_{\mathrm{V}})+\hbar\tilde{\omega}_1]\,[(E_{\mathrm{C}}-E_{\mathrm{ex}})+\hbar\tilde{\omega}_2^*]\,[(E_{\mathrm{ex}}-E_{\mathrm{V}})-\hbar\tilde{\omega}_3]\,[(E_{\mathrm{ex}}-E_{\mathrm{V}})-\hbar\tilde{\omega}_1]} + \\
& + \frac{|D_y^{\mathrm{VC}}|^2\,[(E_{\mathrm{ex}}-E_{\mathrm{C}})+2\hbar\tilde{\omega}_1]}{[(E_{\mathrm{C}}-E_{\mathrm{V}})-\hbar\tilde{\omega}_1]\,[(E_{\mathrm{C}}-E_{\mathrm{ex}})-\hbar\tilde{\omega}_2^*]\,[(E_{\mathrm{ex}}-E_{\mathrm{V}})+\hbar\tilde{\omega}_3]\,[(E_{\mathrm{ex}}-E_{\mathrm{V}})+\hbar\tilde{\omega}_1]} + \\
& - \frac{D_{yy}^{\mathrm{VC}}\,[(E_{\mathrm{C}}-E_{\mathrm{ex}})+\hbar(3\omega+2i\gamma)]}{[(E_{\mathrm{C}}-E_{\mathrm{ex}})+\hbar\tilde{\omega}_3^*]\,[(E_{\mathrm{ex}}-E_{\mathrm{V}})-\hbar\tilde{\omega}_1]\,[(E_{\mathrm{C}}-E_{\mathrm{V}})+\hbar\tilde{\omega}_2]} + \\
& + \frac{D_{yy}^{\mathrm{CV}}\,[(E_{\mathrm{ex}}-E_{\mathrm{C}})+\hbar(3\omega+2i\gamma)]}{[(E_{\mathrm{C}}-E_{\mathrm{ex}})-\hbar\tilde{\omega}_3^*]\,[(E_{\mathrm{ex}}-E_{\mathrm{V}})+\hbar\tilde{\omega}_1]\,[(E_{\mathrm{C}}-E_{\mathrm{V}})-\hbar\tilde{\omega}_2]} + \\
& + \frac{|D_y^{\mathrm{VC}}|^2}{[(E_{\mathrm{C}}-E_{\mathrm{ex}})+\hbar\tilde{\omega}_3^*]\,[(E_{\mathrm{ex}}-E_{\mathrm{V}})-\hbar\tilde{\omega}_2]\,[(E_{\mathrm{C}}-E_{\mathrm{V}})-\hbar\tilde{\omega}_1]} + \\
& + \frac{|D_y^{\mathrm{VC}}|^2}{[(E_{\mathrm{C}}-E_{\mathrm{ex}})-\hbar\tilde{\omega}_3^*]\,[(E_{\mathrm{ex}}-E_{\mathrm{V}})+\hbar\tilde{\omega}_2]\,[(E_{\mathrm{C}}-E_{\mathrm{V}})+\hbar\tilde{\omega}_1]},
\end{aligned}
\tag{17}
$$

and we have used $\tilde{\omega}_1 = \omega + i\gamma$, $\tilde{\omega}_2 = 2\omega + i\gamma$, $\tilde{\omega}_3 = 3\omega + i\gamma$ in the expressions above. Data for the nonlinear coefficients of $MoSe_2$ in the main paper are obtained through Eqs. (12-15).

[1] Andres Castellanos-Gomez *et al.*, "Deterministic transfer of two-dimensional materials by all-dry viscoelastic stamping," 2D Mater. **1**, 011002 (2014).

[2] Diao Li *et al.*, "Polarization and thickness dependent absorption properties of black phosphorus: new saturable absorber for ultrafast pulse generation," Sci. Rep. **5**, 15899 (2015).

[3] Antti Säynätjoki *et al.*, "Ultra-strong nonlinear optical processes and trigonal warping in MoS_2 layers," Nat. Comm. **8**, 893 (2017).

[4] Chinh Tam Le *et al.*, "Impact of selenium doping on resonant second harmonic generation in monolayer MoS_2," ACS Photonics **4**, 38–44 (2017).

[5] R. I. Woodward *et al.*, "Characterization of the second- and third-order nonlinear optical susceptibilities of monolayer MoS_2 using multiphoton microscopy," 2D Mater. **4**, 011006 (2017).

[6] Lasse Karvonen *et al.*, "Rapid visualization of grain boundaries in monolayer MoS_2 by multiphoton microscopy," Nat. Comm. **8**, 151714 (2017).

[7] D. J. Clark *et al.*, "Erratum: Strong optical nonlinearity of cvd-grown MoS_2 monolayer as probed by wavelength-dependent second-harmonic generation," Phys. Rev. B **90**, 121409 (2014).

[8] Kyle L Seyler *et al.*, "Electrical control of second-harmonic generation in a WSe_2 monolayer transistor," Nat. Nanotechnol. **10**, 407–411 (2015).

[9] Rui Wang, Hui-Chun Chien, Jatinder Kumar, Nardeep Kumar, Hsin-Ying Chiu, and Hui Zhao, "Third-harmonic generation in ultrathin films of MoS_2," ACS Appl. Mater. Interfaces **6**, 314–318 (2013).

[10] Chinh Tam Le *et al.*, "Nonlinear optical characteristics of monolayer $MoSe_2$," Ann. Phys. **528**, 551–559 (2016).

[11] Xu Zhou *et al.*, "Strong second-harmonic generation in atomic layered gase," J. Am. Chem. Soc. **137**, 7994–7997 (2015).

[12] Corey Janisch *et al.*, "Extraordinary second harmonic generation in tungsten disulfide monolayers," Sci. Rep. **4** (2014).

[13] J Ribeiro-Soares *et al.*, "Second harmonic generation in WSe_2," 2D Mater. **2**, 045015 (2015).

[14] Yilei Li *et al.*, "Probing symmetry properties of few-layer MoS_2 and h-bn by optical second-harmonic generation," Nano Lett. **13**, 3329–3333 (2013).
[15] Leandro M Malard, Thonimar V Alencar, Ana Paula M Barboza, Kin Fai Mak, and Ana M. de Paula, "Observation of intense second harmonic generation from MoS_2 atomic crystals," Phys. Rev. B **87**, 201401 (2013).
[16] Nardeep Kumar, Sina Najmaei, Qiannan Cui, Frank Ceballos, Pulickel M Ajayan, Jun Lou, and Hui Zhao, "Second harmonic microscopy of monolayer MoS_2," Phys. Rev. B **87**, 161403 (2013).
[17] Carlos Torres-Torres *et al.*, "Third order nonlinear optical response exhibited by mono-and few-layers of WS_2," 2D Mater. **3**, 021005 (2016).
[18] Wenhui Wang, Yanling Wu, Qiong Wu, Jiaojiao Hua, and Jimin Zhao, "Coherent nonlinear optical response spatial self-phase modulation in $MoSe_2$ nano-sheets," Sci. Rep. **6**, 22072 (2016).
[19] Philipp Tonndorf *et al.*, "Photoluminescence emission and raman response of monolayer MoS_2, mose2, and WSe_2," Opt. Express **21**, 4908–4916 (2013).
[20] Hong Li *et al.*, "From bulk to monolayer MoS_2: evolution of raman scattering," Adv. Funct. Mater. **22**, 1385–1390 (2012).
[21] Ayse Berkdemir *et al.*, "Identification of individual and few layers of WS_2 using raman spectroscopy," Sci. Rep. **3**, 01755 (2013).
[22] Gui-Bin Liu, Wen-Yu Shan, Yugui Yao, Wang Yao, and Di Xiao, "Three-band tight-binding model for monolayers of group-vib transition metal dichalcogenides," Phys. Rev. B **88**, 085433 (2013).
[23] A. Marini, C. Hogan, M. Grunig, and D. Varsano, "Yambo: an ab initio tool for excited state calculations," Comp. Phys. Comm. **180**, 1392 (2009).